






Article

Small Lava Caves as Possible Exploratory Targets on Mars: Analogies Drawn from UAV Imaging of an Icelandic Lava Field

Lydia Sam ^{1,2,3,*}, Anshuman Bhardwaj ^{1,2,3}, Shaktiman Singh ^{1,2},
F. Javier Martin-Torres ^{1,2,4}, Maria-Paz Zorzano ^{1,5} and Juan Antonio Ramírez Luque ¹

¹ Division of Space Technology, Department of Computer Science, Electrical and Space Engineering, Luleå University of Technology, 97187 Luleå, Sweden; anshuman.bhardwaj@ltu.se (A.B.); shaktiman.singh@ltu.se (S.S.); javier.martin-torres@ltu.se (F.J.M.-T.); maria-paz.zorzano.mier@ltu.se (M.-P.Z.); juan.antonio.ramirez.luque@ltu.se (J.A.R.L.)

² School of Geosciences, University of Aberdeen, Meston Building, King's College, Aberdeen AB24 3UE, UK

³ National Space Science and Technology Center, United Arab Emirates University, P.O. Box 15551, Al Ain, Abu Dhabi, UAE

⁴ Instituto Andaluz de Ciencias de la Tierra (CSIC-UGR), Armilla, 18100 Granada, Spain

⁵ Centro de Astrobiología (INTA-CSIC), 28850 Torrejón de Ardoz, Madrid, Spain

* Correspondence: lydia.sam@abdn.ac.uk

Received: 14 May 2020; Accepted: 17 June 2020; Published: 19 June 2020



Abstract: Volcanic-aeolian interactions and processes have played a vital role in landscape evolution on Mars. Martian lava fields and associated caves have extensive geomorphological, astrobiological, and in-situ resource utilization (ISRU) implications for future Mars missions which might be focused on subsurface exploration. Although several possible cave “skylights” of tens to >100 m diameter have been spotted in lava fields of Mars, there is a possibility of prevalence of meter-scale features which are an order of magnitude smaller and difficult to identify but could have vital significance from the scientific and future exploration perspectives. The Icelandic volcanic-aeolian environment and fissure volcanoes can serve as analogs to study lava flow-related small caves such as surface tubes, inflationary caves, liftup caves, and conduits. In the present work, we have tried to explore the usability of unmanned aerial vehicle (UAV)-derived images for characterizing a solidified lava flow and designing a sequential methodology to identify small caves in the lava flow. In the mapped area of ~0.33 km², we were able to identify 81 small cave openings, five lava flow morphologies, and five small cave types using 2 cm/pixel high-resolution images. The results display the usefulness of UAV imaging for such analogous research, and also highlight the possibility of the widespread presence of similar small cave openings in Martian lava fields. Such small openings can facilitate optimal air circulation within the caves while sheltering the insides from physical weathering and harmful radiations. Using the available best resolution remote sensing images, we extend the analogy through the contextual and geomorphological analysis of several possible pit craters in the Tharsis region of Mars, in a region of extremely vesicular and fragile lava crust with pahoehoe-type morphology. We report two possible pit craters in this region, with diameters as small as ~20 m. The possibility that such small cave openings can lead to vast subterranean hollow spaces on Mars cannot be ruled out considering its low gravity.

Keywords: lava field; Iceland; caves; Mars; UAV; high-resolution imaging; geomorphology

1. Introduction

Subsurface environments on Mars are expected to provide shielding from space radiation with controlled diurnal temperature variations [1,2]. Additionally, in the case of caves, these semi-opened protected environments may have micro-climates where the relative humidity and temperatures may allow for the stable existence of liquid briny water [3]. Therefore, subsurface will possibly be the focus of the next phases of Mars exploration owing to its significance for astrobiology [4–7], in-situ resource utilization (ISRU) [8], and future human exploration [3,9]. Unlike exposed surfaces, caves, regardless of their dimensions, display steady geophysical, environmental, and geochemical conditions, suitable for habitation and life in extreme extraterrestrial conditions [10]. For example, caves demonstrate a moderate diurnal thermal range and a steadier seasonal regime of temperatures than on the open surface environments. They are well-protected from physicochemical decay triggered particularly by fluvio-aeolian processes and strong fluxes of high intensity ultraviolet, cosmic, and solar ionizing radiations [9]. Subsurface caves such as lava tubes, piping caves, and sub-ice volcanic caves may provide options to perform profiling of paleogeology, paleoclimate, astrobiology, and mineralogy from surface to tens or hundreds of meters subsurface [9]. Moreover, lava caves on Mars can be abundantly icy [11,12] beyond certain depths and can act as a long-term freshwater source to support any habitation [13]. Because of their environmental conditions that favor habitability which may allow for Earth-like life forms to survive, caves have been considered as potential “Special Regions” on Mars, and thus, require dedicated measures for planetary protection [1,3]. In addition to enormous time and budgetary constraints in making artificial subsurface habitats, there are numerous technical difficulties and unknowns associated with drilling to reach the subsurface [14,15]. Thus, having access to this subsurface environment through the natural cave openings could facilitate the easier implementation of any future Mars subsurface exploration program.

Certainly, there are several constraints and aspects to be considered while conducting remote sensing-based research on Martian caves. First, spotting and confirming such cave openings or ‘skylights’ in remote sensing images is difficult. It was only in the previous decade that several such skylights of 100 to 252 m diameter were spotted and confirmed using both, visible and thermal orbiter images for the first time in the Arsia Mons region on Mars [16,17]. Thus, multiple remote sensing datasets in various wavelengths ranging from visible to microwave spectrum and of suitably high spatial resolutions are needed to confirm the existence of such caves. Second, even if we can identify and confirm such caves or lava tubes using orbiter remote sensing platforms, they cannot be straightaway projected as the sites of future Martian settlements or exploration simply because it is even more difficult to ascertain through remote sensing whether a particular tube or cave will be structurally sound and approachable. Third, we need to consider the lower Martian gravity, which is almost 0.38 of Earth’s gravity, and thus could have allowed the formation of larger underground caves following the past volcanic activities. This means that while we are more enthusiastic about the larger skylights and associated tubes, we should also consider the Martian equivalents of smaller terrestrial lava cave types such as surface tubes, inflationary caves, conduits, and liftup caves. The opening of these cave types on earth usually displays diameters of several tens to hundreds of centimeters while they can be of several meters in lengths [18]. Due to the lower gravity of Mars, the equivalents of such smaller terrestrial caves can be up to an order of magnitude larger but still be hard to resolve in meter-resolution images. Nonetheless, these dimensions are substantial enough to consider such smaller caves too as the potential targets of astrobiological and ISRU interests. Thus, what we refer to as “small” lava caves here is a relative term and should be considered with respect to the geographical setting and evolution of the parent lava flow.

To characterize the lava cave entrances in an environment such as that of Mars, it would be extremely important to understand the lava flow surface morphology, recognizing features of a lava flow that may harbor a cave. We have provided several of these details on morphological interpretations with respect to our observations in our Results and Discussion section. However, there are several notable works which provide a detailed background for an interested reader. Calvari

and Pinkerton [19,20] surveyed and provided useful details on lava tube morphology and lava flow emplacement mechanisms for Mount Etna. They produced evidence of a strong relationship between developed tumuli, vents, lava tubes, and parent lava flows in terms of their relative emplacement and significant role in enabling the wider lava spread, further proving the importance of lava tubes in the evolution of extensive pahoehoe and aa flow fields. Duncan et al. [21] further reported on the types and development of tumuli in the 1983 aa flow for Etna. They presented several skylights in aerial and field photographs with a description of their morphologies. Favalli et al. [22] employed an unmanned aerial vehicle (UAV)-based survey to characterize the 1974 Etna lava flows at unprecedented resolutions. They reached an important conclusion that forms the basis for our study as well, i.e., the obtained high-resolution terrain data from UAVs resolves surfaces at submeter resolution, making the identification of folds and small openings possible. Similar works on the morphological characterization of lava flows have been done for Kilauea Volcano, Hawaii. Hon et al. [23] and Peterson et al. [24] provided the evidence that after the formation of lava tubes in Kilauea flow, the flow velocities could reach up to several kilometers per hour compared to a slower moving front, and the tube formation provided an efficient means of lava transport. Kauahikaua et al. [25] further described the lava tube morphology of Kilauea pahoehoe flow by providing dimensional details; lava tube heights varied from 1–20 m depending on the slopes of the terrain and the tubes showed nearly elliptical cross-section with widths several times more than the heights. Orr et al. [26] provided some interesting observational details of sinuous tumuli formation on a lava tube in Kilauea flow. Based on morphological similarities, they also proposed these sinuous tumuli as analogs for possible sinuous ridges in the Tharsis volcanic province on Mars.

The lava fields on Mars have experienced continuous transformations throughout its geological history owing to past volcanic-aeolian interactions and ongoing aeolian erosional/depositional processes [27,28]. The aeolian dunes on contemporary Mars are largely taken as evidence of past volcanism [29,30]. Thus, volcanic and aeolian landforms and processes on Mars are considerably interconnected as the contributors to its landscape evolution. It is this strong interconnection that requires identifying a similar terrestrial setting to perform analogous Mars research related to smaller lava caves. Iceland provides an analogous environment that significantly displays such volcanic-aeolian interlinking and has about 15,000 km² of active sandy deserts which consist of volcanic materials along with its vast lava fields [31]. These Icelandic lava fields are known to harbor several well-explored huge lava tubes/caves [5,32–34]. Additionally, the Icelandic lava flows are also reported to display various types of small caves [18]. For example, lava rise caves usually display a crust of 40–50 cm over an opening of 90–120 cm, pressure ridge caves exhibit a height of ~1 m, lava tumulus caves can be up to several meters long with an entrance of ~50–130 cm height, and gas blister caves can only be of a few centimeters to several meters in dimensions [18]. Detection, mapping, and morphometry of such small caves require extremely high-resolution imaging and photogrammetry, which is possible using a UAV. UAVs, as an aerial remote sensing platform, act as a bridge between spatially discontinuous, costly, and time-consuming field observations and spatially continuous but costlier and coarser spaceborne remote sensing [35,36]. Realizing such research prospects of using UAVs for Mars research, the National Aeronautics and Space Administration (NASA) is sending the first UAV to Mars with the agency's Mars 2020 rover mission, which is currently scheduled to launch in July 2020 [37]. As one of the initial works to employ a UAV for active volcano monitoring, Nakano et al. [38] studied the landform evolution using high-resolution images in the wake of the Nishinoshima volcano eruption in Ogasawara Islands in November 2013. This volcanic eruption formed and enlarged a new island, and the UAV-derived digital terrain model (DTM) and orthomosaic helped in estimating the area and volume of the new island. Turner et al. [39] employed UAV flights for lava flow hazard prediction and repeat monitoring of the 2014–2015 Pāhoehoe lava flow crisis, Hawaii. They generated a series of 1 m resolution DTMs and associated paths of steepest descent over the study area. The modeled flow paths for future eruptions showed the possibility of deflection of future flows by the newly emplaced lava, thus possibly threatening new communities in the surrounding regions. In the present research,

our objective was to employ UAV imaging to derive high-resolution orthomosaic and morphometric information about a part of the lava flow as an analog site to study small lava caves. To the best of our knowledge, there is a lack of any published study surveying a lava flow full of small lava caves as a Mars analog environment, by employing UAV-based high-resolution 3D and morphometric mapping to suggest the methods of identifying the small cave openings. We hypothesize that small caves might be abundant on Mars but are challenging to find due to the present-day spatial resolution limitations of space-borne remote observations and also due to the prevalent dust obscuring the underlying land features. A recent research article [40] provides evidence of the presence of small voids or caves in possible Martian mudflows that propagate and appear like terrestrial pahoehoe lava flows.

As detailed above, the common lava flow morphologies on Earth are well-explored, and in our research, we do not intend to discover a new morphology. Instead, we aim to highlight how UAV imaging can improve our visualization and understanding of the lava terrain and morphologies at unprecedented resolutions covering large spatial domains. A vast majority of the previous studies on the morphological characterization of lava flows have been either mostly field-based with spatial discontinuity or helicopter/aircraft aerial imaging-based with coarser spatial resolutions. As a result, the wide distribution and frequency of possible small cave openings/folds, or the submeter three-dimensional terrain parameters, which we have characterized for a confined portion of the huge lava flow, are significant in highlighting the prospects of high-resolution and high-quality images for geomorphology research. In addition, in the following sections, we have provided ample horizontal perspective views in form of field photographs using high-zoom tripod-based cameras to depict and verify the discussed morphologies and cave openings in the aerial orthomosaic obtained from vertical nadir viewing. Thus, the purpose of our work is to define a terrestrial analog that may help to understand the frequency of formation of small cave openings/folds in lava environments and further understanding their typical geomorphological features. We base our analysis on high-resolution remote sensing observations of a terrestrial analog and use ground-based validation to assess the limitations and potential of our proposed mapping to extrapolate or infer the true conditions which may be found on Mars. Finally, based on this method we present the detection of a few Martian small-sized possible caves openings which seem to have similar characteristics to the ones found in the terrestrial analog environment. Thus, the present study aims at filling the research gap with the following objectives:

1. To perform UAV-based high-resolution imaging survey for the part of a lava flow showing all the main morphologies and abundance of small caves;
2. To design a sequential methodology for identifying and characterizing the small cave openings on the UAV images with respect to the lava flow morphology;
3. To perform a high-resolution comparison of the Icelandic lava flow with some examples from Mars.

In the subsequent sections, we briefly introduce the study area. We also provide details on the methods of high-resolution UAV imaging, 3D terrain generation, morphometric analyses, and cave identification. We further discuss the implications of our results for the possible small lava caves on Mars.

2. Study Area

The selection of the study area was based on five main requirements. First, there was a need to have an appropriate UAV launch site approachable, flat, and close enough to the area of interest. Second, the area of interest had to be away from the regular walking paths and banned for direct approach to observe solidified lava flow and caves in their natural environment without any anthropogenic factor affecting the terrain. Third, the drone flying over the area of interest and the remote controller at the launch site had to be in direct line-of-sight all the times without any hillock in between to ensure uninterrupted control and flight. Fourth, the area had to display noticeably changing elevation and topography of lava flow for observing varying frequency of caves with respect to the topography. Fifth, the study area needed to cover all main morphology classes of the lava field.

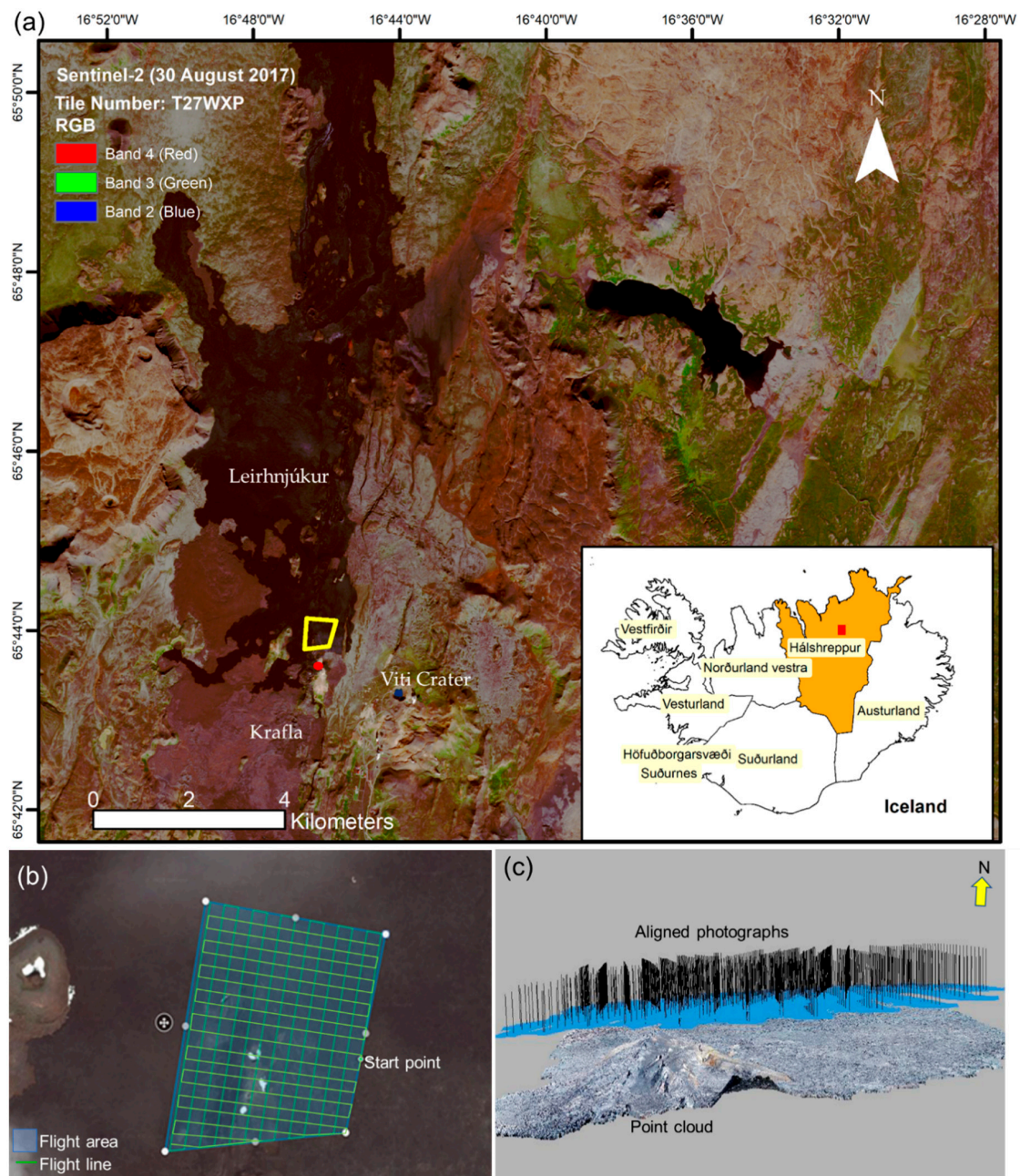


Figure 1. Location map and flight details: (a) contextual map of the study site in true color composite (RGB:432). The red rectangle in the inset political map in (a) shows the geographical location of the study site in Iceland. The yellow quadrilateral shows the relative position of the flight site. The red dot shows the unmanned aerial vehicle (UAV) launch site; (b) area of interest and the flight lines in a double grid format; (c) aligned photographs and dense point cloud for the study area for the survey on 11 July 2018. Image credit for (a): map generated using European Space Agency’s (ESA’s) Sentinel-2 multi-spectral instrument (MSI) remote sensing data acquired under the European Commission’s Copernicus Programme and downloaded from United States Geological Survey (USGS) EarthExplorer. Image credit for (b): the flight lines are produced using Pix4Dcapture flight planning freeware with the Google Earth (GE) image in the background and the data provider for the GE image is CNES/Airbus. Image credit for (c): image generated using Agisoft PhotoScan Pro standalone licensed software.

Considering these requirements and the acquired permission from the authorities for the fieldwork, we opted for imaging a part of the Leirhnjúkur fissure volcano lava field, situated in Krafla Caldera of

Iceland (Figures 1 and 2). This lava field is known for the presence of vent caves formed by upwelling and withdrawing of the basalt lava directly from the magma chamber [32,34]. Although the surface openings of these vent caves are rather small (1–2 m wide), they widen out towards the bottom reaching up to 4–5 m in dimensions [18,32], and thus, perfectly match the premise of our research objectives. The measured average height of this lava flow is 6 m above its surroundings at the flow margins [34]. However, a knowledge of pre-flow topography confirms the presence of considerable topographic depressions at several places, thus indicating an average lava flow thickness of 11 m [34]. The lava field is predominantly shelly-type formed by very vesicular pahoehoe lava with fragile lava crust, flow lobes, and small lava tubes which eventually became hollow inside due to downslope draining or degassing [34]. However, our area of interest equally consisted of the slabby pahoehoe lava flow. The rifting episode in the Krafla caldera is known as “Krafla Fires” and it lasted between 1975 and 1984 [34,41]. This region was modified by a series of fissure eruptions during 4–18 September 1984 [34]. We further considered the most recent map presented in Figure 2 of Aufferistama et al. [42] for deciding the boundary of the area of interest to ensure that it covers all the main morphology classes of the lava field, i.e., spiny pahoehoe, slabby pahoehoe, shelly pahoehoe, rubbly aa, and cauliflower aa.

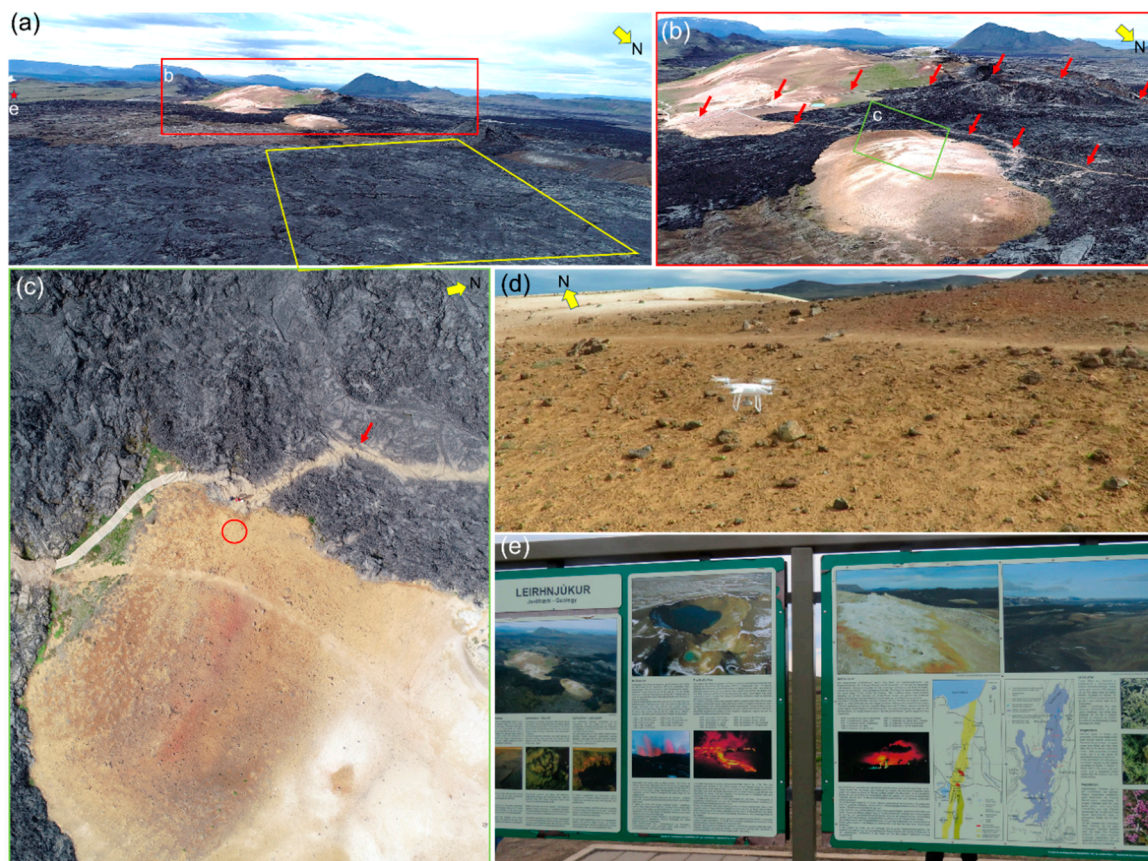


Figure 2. Several of the field photographs: (a) aerial shot was taken from the farthest position of the UAV facing the launch site while surveying. The red rectangle provides a context for (b). The yellow quadrilateral highlights the area of interest as shown in Figure 1a. The red star near the upper left margin in (a) provides a context for (e); (b) closer shot of the elliptical tourist trail (red arrows) and the launch site (green rectangle); (c) Nadir view of the launch site (red circle) and the tourist trail (red arrow); (d) UAV during the lift-off from the launch site; (e) information board for Leirhnjúkur fissure volcano at the tourist parking site.

3. Materials and Methods

The following methodological steps were taken to achieve the research objectives.

3.1. UAV Imaging System

We used a DJI Phantom 4 Pro quadcopter (Figure 2d) for the study. This UAV weighs ~1.4 kg inclusive of the battery and propellers. The diagonal dimension (excluding the propellers) is 35 cm. It can fly for a maximum duration of ~30 min. The drone can be flown up to a height of ~6000 m above sea level (asl). However, in the present study, we flew it below ~650 m asl at all the times. The UAV can fly within a maximum wind speed of 10 m/s and a temperature range of 0°–40°C. The wind speed in the highlands of Iceland can be extremely high during a larger part of the day and therefore depending on the weather forecast, we planned the flights between 11 am and 12:30 pm local time on 11 July 2018 with a wind speed of 2–3 m/s and a temperature of 15 °C. The UAV is equipped with an integrated 3-axis gimbal that provides an extremely narrow angular vibration range ($\pm 0.02^\circ$) and always maintains the preferred camera look-angle as per our preference. DJI Phantom 4 Pro uses both global positioning system (GPS) and global navigation satellite system (GLONASS) satellites and operating frequencies of 2.4–2.483 GHz and 5.725–5.825 GHz, which provide it a high hover accuracy range with respect to GPS positioning (vertical: ± 0.5 m; horizontal: ± 1.5 m) up to 7 km from the launch site. However, in the areas with undulating topography and dense vegetation, it is better not to send the UAV too far from the launch site and in our case, the UAV was sent up to a maximum aerial distance of 1200 m from the launch site.

The DJI Phantom 4 Pro camera produces photographs with standard RGB channels using a 1" complementary metal-oxide-semiconductor (CMOS) sensor. The 20-megapixel sensor has a manually adjustable aperture from F2.8 to F11, supporting autofocus with a focus range from 1 m to infinity. The sensor has a field of view (FOV) of 84° and the mechanical shutter facilitates still imaging for fast-moving UAV or object of interest. This camera sensor captured georeferenced images at a high spatial resolution of <2 cm/pixel, even from a flying altitude of 70 m for our study. This UAV system was recently successfully employed for another Mars analog research to study seasonal brines [43].

3.2. Flight Planning to Mitigate Systematic Error in Absence of Ground Control Points (GCPs)

The main requirement of our work was to obtain high-resolution overlapping images to make extensive visual observations related to cave openings and to perform terrain modeling for generating orthomosaic of the area of interest within an undisturbed solidified lava field using structure-from-motion (SfM) photogrammetry [44]. This meant that we had to opt for a pristine area of interest which was approachable to fly the UAV and yet banned for a direct human approach. This was needed to capture the part of the lava field in its natural setting where the solidified lava flow had been modified primarily through natural processes during the past three and half decades after the last eruptions, to propose a reliable analogy with Mars. However, this also meant that we were not permitted to acquire ground control points (GCPs) using a differential global positioning system (DGPS) unit to ensure very high positional accuracy of the obtained DTM and orthomosaic. Nevertheless, this did not put a constraint on deriving relevant inferences for our research objectives as more than high positional accuracy, i.e., exact latitude, longitude, and elevation, we were interested in mitigating systematic errors for achieving high relative accuracy and in deriving terrain derivatives such as slope, roughness, and elevation profiles for morphometry. High relative accuracy refers to the same relative distance between any two points on the modeled terrain and the distance between those points on real earth terrain. Although with the same flying plan settings as used in the study (Table 1), we later tried to estimate the positional accuracy of the generated DTM for our UAV system with respect to Trimble R10 Integrated Differential Global Navigation Satellite System (DGNSS) System. The obtained root mean square error (RMSE) was ~5 m in vertical and ~2 m in horizontal; sufficient enough for our objectives which are independent of the requirement of the absolute positional accuracy and mainly focused on high-resolution imaging of the terrain. This range of RMSE is reported by another recent study [45] for similar flight plans like ours.

Table 1. Flight plan and image parameters.

Parameter	Value
Flight altitude	70 m
Flight plan	Double grid
Battery used/flight	1
Side overlap	80%
Front overlap	85%
Camera Angle (from vertical)	0°, 20°
Total flight time/flight	~16 min
Total area captured	~334,000 m ²
Total images captured	990

Systematic vertical errors arise mainly due to a combination of near-parallel imaging directions and inaccurate correction of radial lens distortion [46] and affect the relative elevation between two points within a DTM by producing a “vertical doming” of the surface [46]. In the absence of GCPs, such errors can still be significantly reduced through the collection of oblique imagery [46,47]. Images acquired on orthogonal routes at 20°–30° inclination to the vertical combined with images acquired at 0° inclination to the vertical (nadir view), and with high along-track and across-track overlaps have been reported to considerably minimize both positional and systematic errors in absence of GCPs [45,46]. Our flight planning was also in accordance with such considerations (Table 1).

The area of interest could not be completely covered in one flight and on a single battery. Moreover, we had to choose an orthogonal dense flight plan and obtain oblique imagery as well with a tilted camera, meaning higher battery consumption. Therefore, we decided to cover the area of interest in two overlapping flight plans. We made two flights (at 0° and 20° tilt from vertical) for each of the two segments of the study area, thus four flights in total. Table 1 highlights the various flight plan and image parameters that we employed in the Pix4Dcapture flight planning freeware app during the field data acquisition. Pix4Dcapture provides the option to allow tilted image acquisitions as per our requirements. Additionally, this freeware also gives options for a flight plan called “double grid” (Figure 1c) which is an orthogonal dense flight plan as we required. The launch and landing sites were the same for all the flights. To increase the density and accuracy of the point clouds and stereo-imaging, we ensured a high degree of overlap (side overlap = 80% and front overlap = 85%) between the images.

3.3. Generation of DTM and Orthomosaic

We used Agisoft PhotoScan Pro stand-alone licensed software for processing the aerial photos to generate the DTM and orthomosaic using SfM photogrammetry. For SfM processing, Agisoft PhotoScan Pro is a proven performer amongst several widely used software packages, such as EyeDEA (University of Parma), ERDAS-LPS, PhotoModeler Scanner, and Pix4UAV [48] and has been widely used in a variety of environmental research in recent years (e.g., [43,49–52]). Agisoft PhotoScan Pro has a fully automated workflow for 3D reconstruction and, in addition to its proven capability for robust surface modeling (e.g., [48]), it can derive sensor parameters intrinsically to perform calibration and local processing to generate outputs in multiple file-formats compatible with other geospatial software [49]. The intrinsic SfM processing in PhotoScan is detailed in a paper by Verhoeven [53]. Here, we briefly highlight the three main processing steps for deriving the DTM and orthomosaic from the aerial survey data using Agisoft PhotoScan Pro:

1. Photograph alignment (bundle adjustment): Agisoft PhotoScan aligns the photos from a UAV survey using the camera location coordinates and algorithms, automatically detects stable common features among the overlapping images, and determines the location and alignment of each camera position with respect to others [48,49]. This process of bundle adjustment generates a 3D sparse point cloud using the stereo-imaging, projection, and intersection of pixel rays from the different positions [49]. Using a very high computing hardware system (Intel Xeon E5-2650 v4,

12 cores, 24 threads central processing unit, 256 GB random-access memory, and Nvidia Geforce Titan XP 12 GB GDDR5X graphics card), we employed highest processing parameters within Agisoft PhotoScan workflow to derive the best possible results. For photograph alignment, we opted for the “Highest” accuracy and the highest possible numbers of tie points and key points in the processing tool window. The results of the alignment process are shown in Figure 1c.

2. Geometry building and dense point cloud generation: A densification technique is applied within the software on the already generated sparse point cloud through the bundle adjustment to derive a 3D dense point cloud using multi-view stereopsis (MVS) or depth mapping techniques [54]. The model geometry is corrected by the intrinsic process of matching features to complete the final phase of geometry building to generate an accurate high-resolution 3D dense point cloud [49]. For this step, we opted for the “Ultra high” processing parameter and “Aggressive” depth filtering to derive the best possible results.
3. Texture building and DTM generation: In this step, the generated 3D dense point cloud provides a continuous surface that can be triangulated and rendered with the original imagery to build a textured 3D mesh and create the final DTM [49] and, subsequently, the orthomosaics. For the DTM generation, the dense point cloud was selected as the source data, with enabled interpolation and a pixel resolution of 2 cm/pixel, and WGS 1984 UTM Zone 28N was assigned as the coordinate system for the final outputs. For orthomosaic generation, the DTM were selected as surface data, with enabled hole filling and 2 cm/pixel output resolution.

3.4. Morphometry

Deriving geomorphometric parameters to study the terrain of a lava field can provide extremely useful information [55]. We derived terrain derivatives, such as the slope, aspect, and surface roughness, for morphometric analyses (e.g., [56–61]). We derived the slope and aspect parameters using the Spatial Analyst toolbox of the ArcGIS software version 10.6.1. The Slope tool computes the maximum rate of change in elevation value for a given elevation pixel, from that pixel to its eight contiguous pixels [58,62]. The Aspect tool calculates the alignment of the surface slope as the maximum rate of change from each pixel to its eight neighbors [58,62]. We used the Roughness tool within the Geospatial Data Abstraction Library (GDAL) of QGIS 2.18.23 software to derive the roughness parameter. The Roughness tool accepts the modeled elevation surface as input and calculates the largest inter-cell difference of a central pixel and its surrounding pixels for each of the pixels in the surface raster [63]. We further employed the Reclassify tool within the Spatial Analyst toolbox of ArcGIS 10.6.1 to categorize the aspect parameter into suitable classes. The classification schemes for aspect is explained in the respective tool help sections of the ArcGIS 10.6.1 software. The Spatial Analyst toolbox was also used to classify elevation into three classes using the “Natural Breaks” option as this classification is based on natural groupings that are inherent to the data and classes are identified based on similar values and maximum differences between classes [64].

3.5. Cave Identification

UAVs provide access to areas that are hard to reach and/or dangerous, such as vertical or overhanging rock outcrops or gas-rich and unstable volcanic areas. The present study demonstrates the scientific and operational potential of UAV-derived high-resolution orthoimage and DTM to detect and identify probable lava cave openings. To correctly identify and map cave openings, we adopted a methodology taking into account the 3D model of the surface along with visual interpretation (Figure 3).

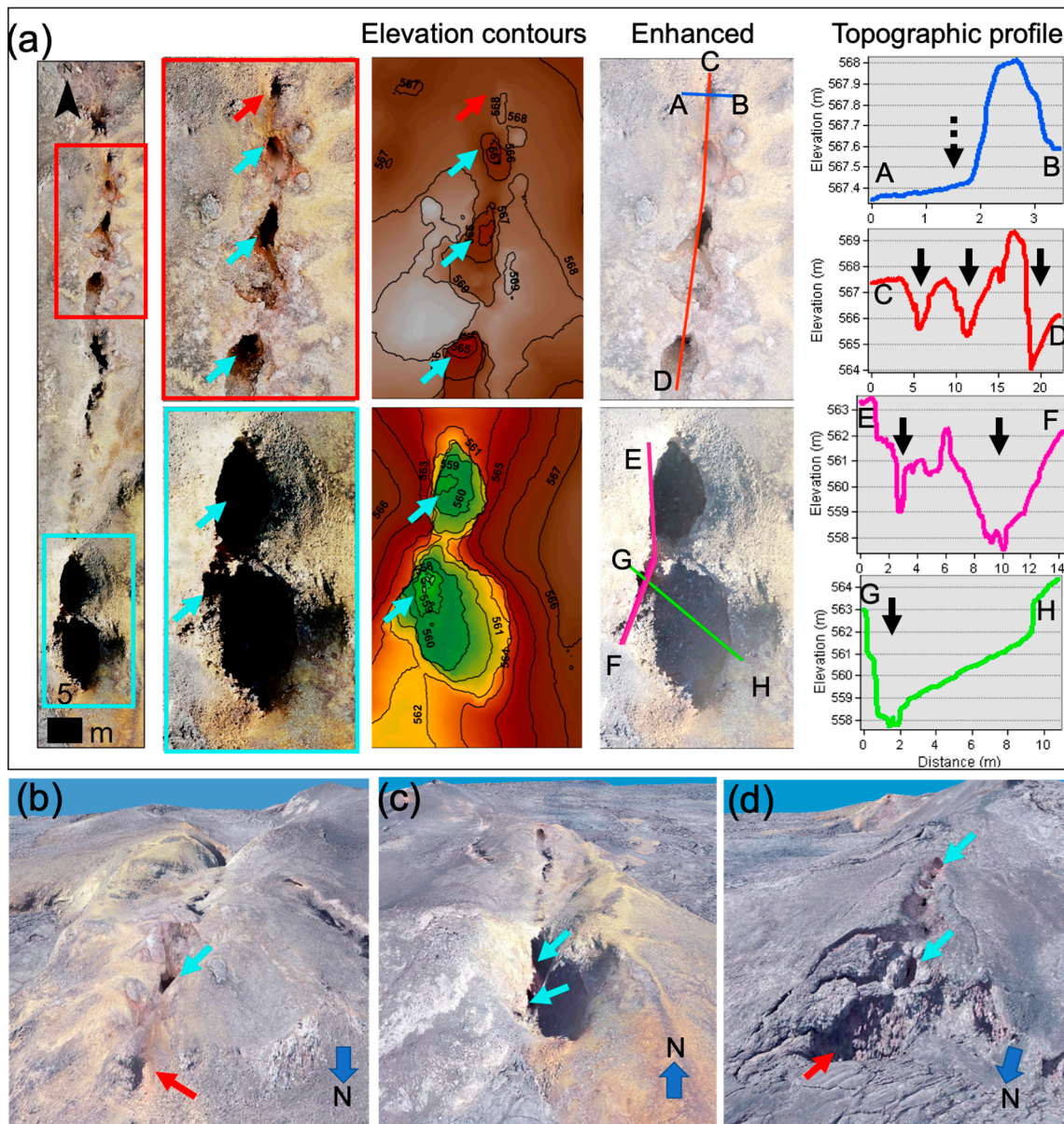


Figure 3. Cave opening identification strategy: (a) our systematic approach using DTM and contours, histogram enhanced image, and topographic profiling for identifying cave openings, illustrated here for a collapsed lava channel; (b) use of 3D perspective view to confirm the dark pixels (red arrow) in orthomosaic shown within the red rectangle in (a) as a shadow caused by topography, whereas the cyan arrow depicts one of the possible cave openings; (c) use of 3D perspective view to confirm the dark pixels (cyan arrows) in orthomosaic shown within the cyan rectangle in (a) as cave openings; (d) 3D perspective view of another collapsed lava channel with openings and shadows. Cyan and black arrows in all the figures represent confirmed cavities in images and profiles, respectively. Red and dotted black arrows show spots that are not cave openings, but are shadows caused by topography in images and profiles, respectively.

For this purpose, first, the DTM of the region of interest was used to understand the topographic pattern and the direction of the slope. The use of contour lines overlaid on the orthomosaic and DTM proved to be useful in distinguishing several of the caves from topographic shadows. In cartography, a contour line (often called a “contour”) joins points of equal elevation above a given level, such as mean sea level. Often in topographic analysis, the trend of the contours is taken into account overlooking the values of each contour. For our analysis, the contour lines were overlaid and labeled so that the values

can be compared for correct identification. In addition to precision, this technique also ensured that the shadows would not be misinterpreted as cave openings using solely visual interpretation. The elevation contour panel of Figure 3a elucidates the effectiveness of this approach as the decreasing contour lines can be seen forming concentric curves around the cave openings. Second, we performed contrast stretch and histogram enhancement on the orthomosaic to try and visualize the terrain within shadow for confirming if it is an opening. The histogram enhanced images in Figure 3a can be observed in comparison with the corresponding unenhanced images for reduced darkening caused by topographic shadow. Third, topographic profile analysis was performed to further distinguish between cave openings and shadow and it proved to be extremely effective. The topographic profiles presented in Figure 3a highlight the significant dips of 2–5 m for the openings along the transects. The dark pixels marked by the red arrow in Figure 3a were hard to characterize using only contours and histogram enhanced views. However, the profile analysis at once clarified that the dark pixels are just the results of shadow and there was no cave opening present. Fourth, visual interpretation of 3D perspective views of orthoimage draped over DTM was performed to further confirm the ambiguous cases. For example, the red arrow zone shown in Figure 3a was observed in 3D (Figure 3b) from various angles to confirm that it was only a topographic shadow. On the contrary, the 3D perspective view in Figure 3c confirmed the dark pixels marked by cyan arrows within the cyan rectangle in Figure 3a as the cave openings. The fragile part of the roof of a small lava channel could collapse, making a visible entrance to the lava channel, which is called a pit crater [65]. Although the particular features in Figure 3c appear more like open vertical conduits with hornitos [18,66], a contextual look at them confirms them to be part of the same lava channel shown in leftmost panel of Figure 3a. Fifth, limited ground truth was conducted from the closest permissible points of approach to the area of interest using Canon's PowerShot SX740 HS camera with 80× Zoom Lens, wherein observations for different types of cave openings were made and captured. This was especially important to identify the side-facing caves or cave openings below cliffs, which could be hidden from view using only aerial remote sensing. Thus, we analyzed and cross-checked all the identified cave openings using the systematic approach explained above and the adopted methodology is reproducible for any similar future research.

4. Results and Discussion

We present our findings within three broad sections. First, we introduce the typical lava flow morphologies, terrain characteristics, and cave distribution within our region of interest. Second, we discuss the cave types in different lava morphologies and terrain. Third, we discuss possible analogy with Martian lava flows and caves. The following sections summarize the key results of our study within the predefined objectives.

4.1. Lava Flow Morphologies and Terrain Parameters

Lava differs in its composition and thus in its viscosity and depending on the nature of solidified lava flow surfaces, there are mainly two types of flows: (1) pahoehoe, and (2) aa. The pahoehoe basaltic lava displays varying topography in form of smooth, hummocky, and ropy exterior and typically moves as a sequence of small lobes and toes continually breaking out from a cooled crust [67]. The aa lava differs from pahoehoe lava as it displays rough rubbly surface formed by broken block features called clinkers [67]. The high-resolution images and DTM helped us in characterizing all the main lava morphologies as the surveyed terrain was resolved at unprecedented resolution to identify the associated features of various lava flows. Figures 4 and 5 provide the topography and contextual information for the lava flow morphologies and morphometries shown in Figures 6 and 7. Table 2 provides the field photographs and descriptions of these morphologies. The regions presented in Figures 6 and 7 have been selected based on the distinct morphologies to highlight the variations in the terrain parameters. The entire region of interest displayed elevations within a range of ~25 m, i.e., ~553–578 m (Figure 5). We used the Natural Breaks method [64] to classify the DTM into three major elevation classes based on similar values and maximum differences between the classes (Figure 5b).

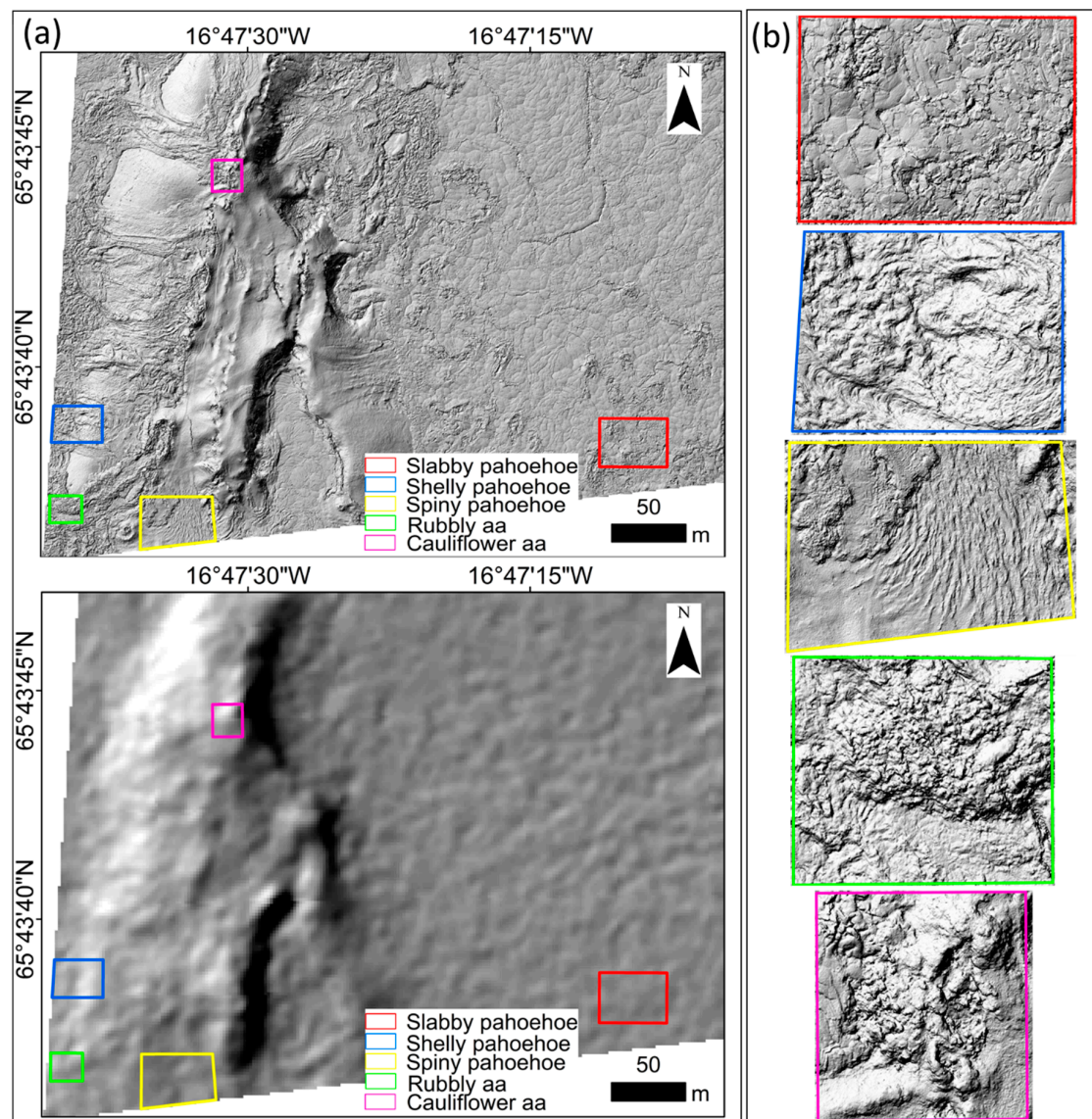


Figure 4. Visual comparisons: (a) between hillshaded views of 2 cm/pixel UAV DTM and 2 m/pixel ArcticDEM [68] (courtesy: Polar Geospatial Center); and (b) among various lava flow morphologies in 2 cm/pixel hillshaded UAV DTM. The quadrilaterals in (a) provide contextual information for (b), Figures 6 and 7.

Figure 4 remarkably highlights the improvement in visual quality and terrain characterization using UAV DTM. We compared the hillshaded views generated for 2 cm/pixel UAV DTM and 2 m/pixel ArcticDEM [68]. The ArcticDEM is the highest resolution open-access digital elevation model (DEM) available for this region and we used the National Land Survey of Iceland web portal [69] to download it. The ArcticDEM is derived from satellite sub-meter stereo imagery such as those of WorldView 1-3 and GeoEye-1, and has a vertical accuracy better than 1 m and the horizontal accuracy of 3 m for our study area [70]. As visible in Figure 4, even the 2 m/pixel hillshaded view generated from the ArcticDEM is not sufficient to enable the lava flow characterization. The visual enhancements in terrain observation presented in Figure 4 confirm the premise of our research, i.e., UAV-derived DTM has the potential to bridge the gap between discrete field observations and spatially continuous but coarser resolution satellite observations for volcanology. A similar resolution limitation was observed and reported by Müller et al. [71] where they could identify centimeter-scale fractures in the Holuhraun eruption site, Iceland, using UAV images, as compared to meter-scale fractures identified using the

WorldView-2 datasets for the same region. The various lava flow morphologies based on the UAV DTM are further discussed in Table 2, Figures 6 and 7.

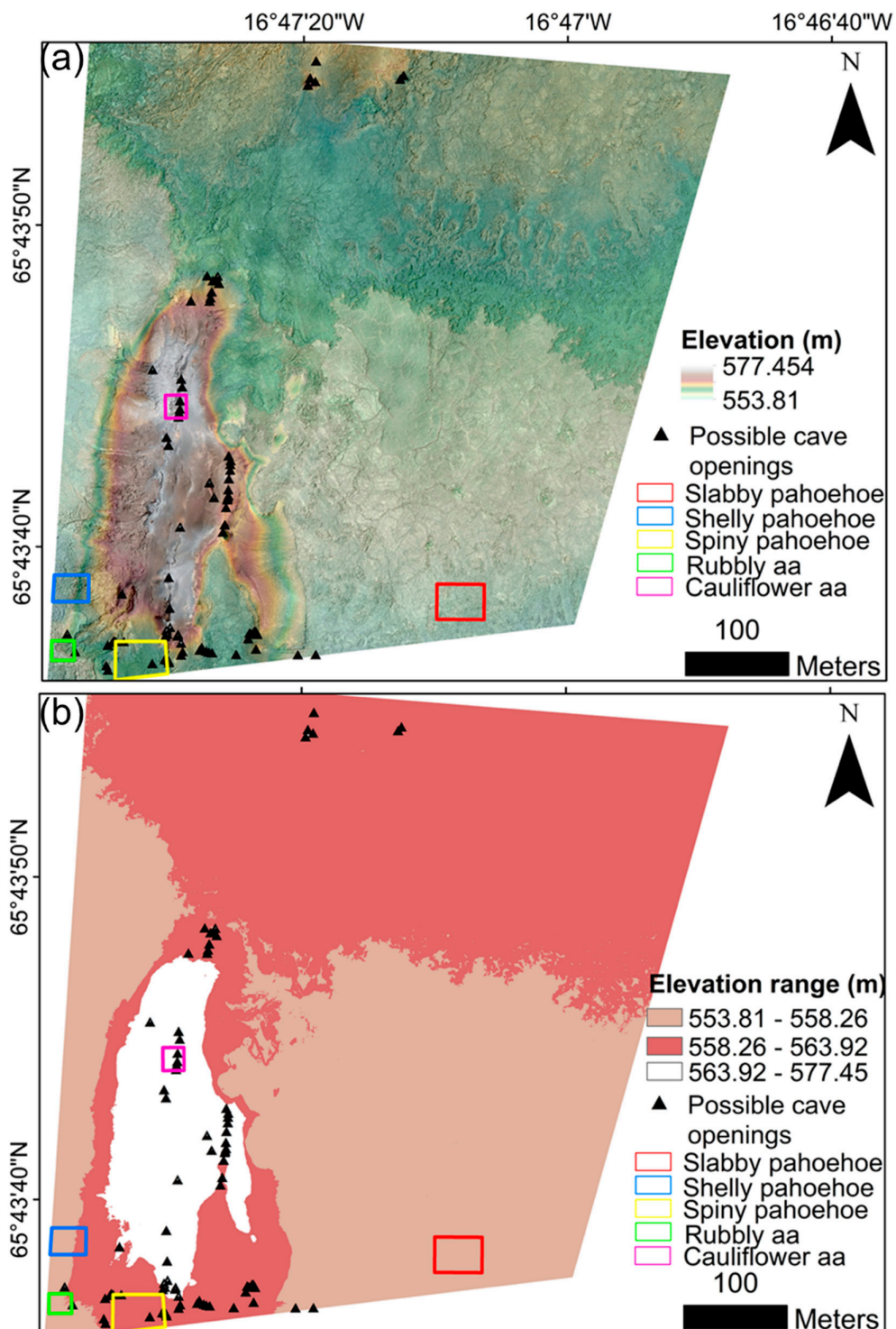


Figure 5. Mapped portion of lava field: (a) high-resolution DTM draped over the orthomosaic with marked possible cave openings and sampled lava flow morphologies; (b) Natural Breaks-based classification of the DTM to highlight the variations in cave opening density and lava flow morphologies within various elevation ranges. The marked rectangles also provide contextual information for Figures 6 and 7.

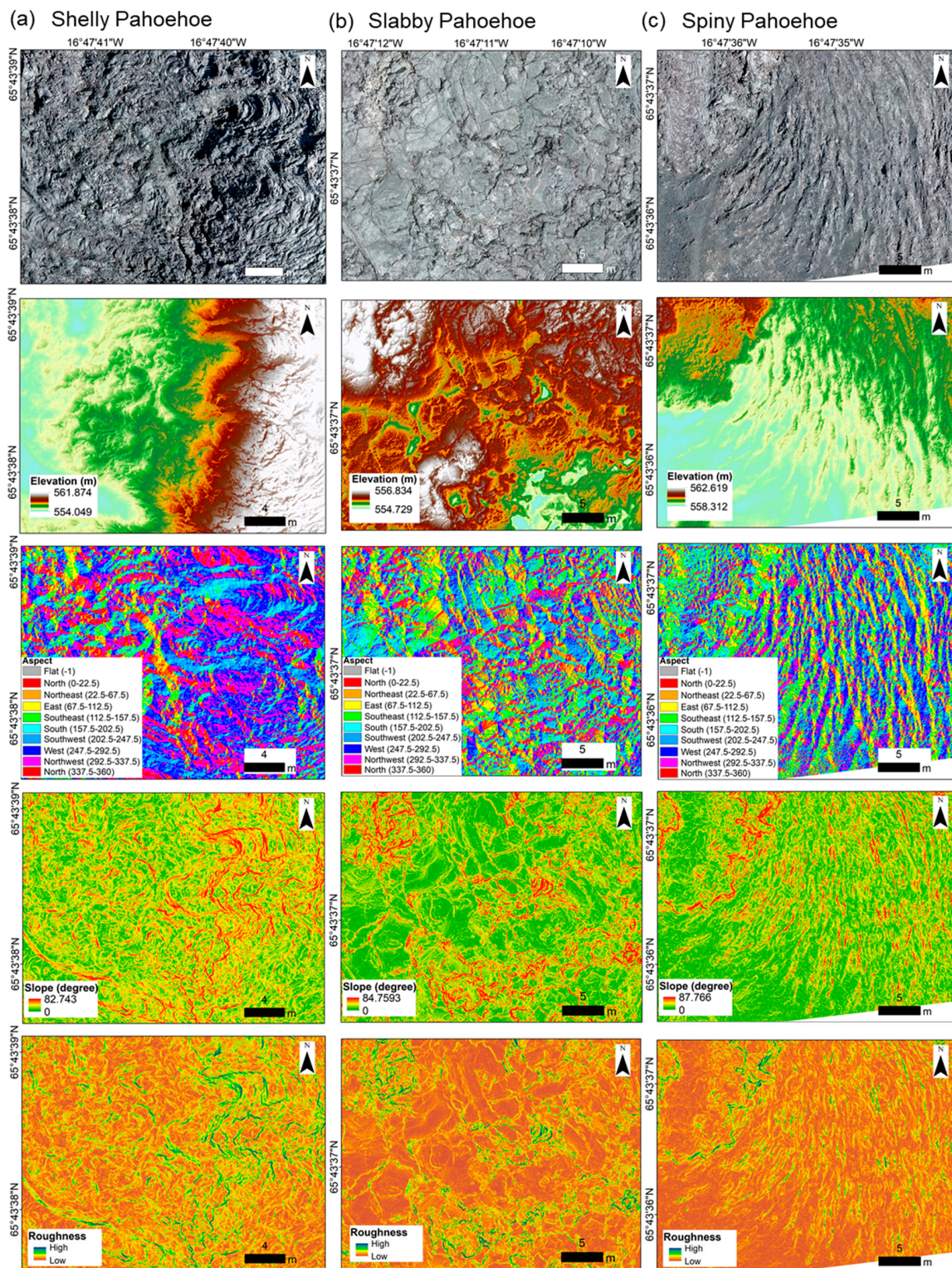


Figure 6. Lava morphologies derived from UAV imaging and photogrammetry for pahoehoe flow at Leirhnjúkur fissure volcano lava field in Krafla Caldera, Iceland: (a) shelly pahoehoe; (b) slabby pahoehoe; (c) piny pahoehoe. The maps represent orthomosaic, elevation, aspect, slope, and roughness in top-to-bottom order.

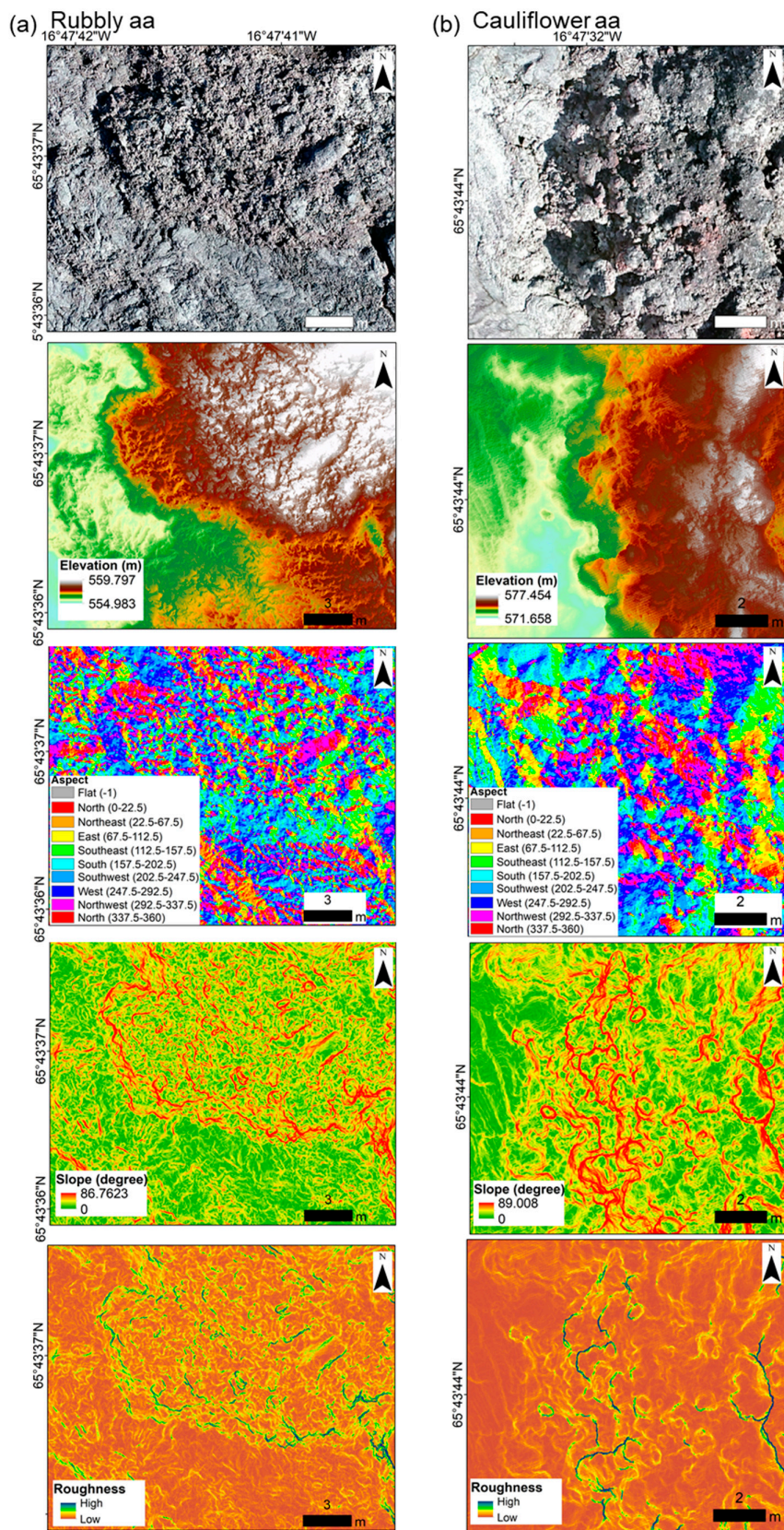
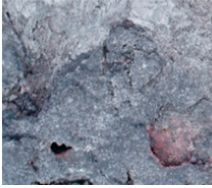

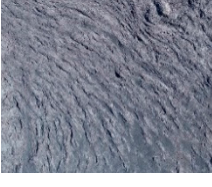
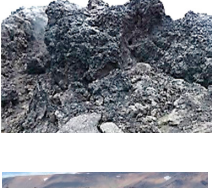



Figure 7. Lava morphologies derived from UAV imaging and photogrammetry for aa flow at Leirhnjúkur fissure volcano lava field in Krafla Caldera, Iceland: (a) rubbly aa; (b) cauliflower aa. The maps represent orthomosaic, elevation, aspect, slope, and roughness in top-to-bottom order.

Table 2. Description of the lava morphology present in the study area.

Lava Morphology	Description	Mean Slope (°)	Mean Roughness (mm)	Field Photo	Reference
1. Pahoehoe lava					
Shelly pahoehoe	Characterized by fragile gas cavities, small tubes, and buckled fragments of the surface crust. Lobes often form the margin of the sheet flow.	23.95	24.93		[34,72]
Slabby pahoehoe	Slabs of broken crust, usually less than a meter to few meters across. Formed when the pahoehoe crust is tilted and stretched during flow.	15.55	15.32		[73,74]
Spiny pahoehoe	Flexible crusts ruck into tight folds before cooling. The smooth glassy surface is the result of its formation under very low strain rates, when the lava is extremely crystalline and viscous. Surface resembles segment of coiled rope.	15.50	13.99		[75–77]
2. Aa lava					
Cauliflower aa	Appears as bulbous protrusions on the lava surface which breaks to give fragments up to decimeters across. Grey-black, often glassy surfaces rough at millimeter-scale. This is an initial aa lava type in the transformation from pahoehoe to rubbly aa.	26.31	30.04		[34,73]
Rubbly aa	Formed as the crust breaks to yield rounded rubble varying in dimensions from sand to blocks several meters in diameter. Have accumulated fragments, with a clinkery and blocky surface.	24.97	27.42		[34,74]

The two types of lava flows are further classified into subclasses based on their inherent morphology. For our region of interest, the lava types observed are (1) shelly pahoehoe, (2) slabby pahoehoe, (3) spiny pahoehoe, (4) cauliflower aa, and (5) rubbly aa. A concise description of these morphologies along with our field photographs and references for interested readers are provided in Table 2. Slabby pahoehoe is the most predominant lava flow morphology within our region of interest followed by shelly pahoehoe and rubbly aa. Spiny pahoehoe and cauliflower aa are confined within the regions marked in Figure 5. The lowest elevation range (~553–558 m) displayed a clear dominance of slabby pahoehoe (Figure 5). Rubbly aa and shelly pahoehoe were observed together in both, lowest and middle elevation zones (~558–564 m) (Figure 5). Spiny pahoehoe was most distinctively observable in middle elevations while cauliflower aa was confined to the top elevation range along with shelly pahoehoe (~564–578 m) (Figure 5).

Slabby pahoehoe is formed when relatively fast-moving pahoehoe flows become more viscous with subsequent heat loss, allowing the molten lava to grab and rip the pahoehoe crust into chunks [75]. The reported dimensions of the slabs usually reach up to several meters across and a few centimeters to decimeters in thickness [74,75]. For our study area, the observed diagonal dimensions for the slabs varied between ~1 and 5 m, and the thickness that we could estimate using the generated DTM varied between ~8 and 15 cm (Figure 6b). Although each of the individual slabs display a smooth exterior, the

arbitrary and cluttered placement of these slabs gives the flows a rough and crusty appearance (Table 2, Figure 6b) [34,74–76]. The estimated mean surface roughness was ~15.32 mm, the second-lowest among the identified flow morphologies. The aspect image in Figure 6b clearly shows this brittle morphology. The largely smooth texture of individual slabs is the reason behind the low mean slope and roughness values of slabby pahoehoe flow in our study area (Table 2).

The smoothest lava morphology, as expected, was of spiny pahoehoe flows with the estimated mean surface roughness of ~14 mm, the lowest among the identified flow morphologies (Table 2, slope and roughness maps in Figure 6c). The smooth glassy surface is the result of its formation under very low strain rates when the lava is extremely crystalline and viscous [23]. However, this smooth topography of gently undulating billows and ropes are at centimeter or coarser scales; on a millimeter-scale, this morphology displays a spiny and granulated surface [23]. The surface resembles a segment of coiled rope and the jumbled aspect map shown in Figure 6c highlights this. Spiny pahoehoe is commonly formed as the leakage from dying or stagnating lobes of pahoehoe flows or from the edges and the fronts of aa flows [75]. The marked adjacency of spiny pahoehoe with shelly pahoehoe and rubbly aa can be observed in Figure 5.

Shelly pahoehoe is the second most predominant morphology within our region of interest. It is an extremely vesicular lava flow morphology with fragile lava crust [23,72,74] and therefore primarily consists of observable small cave openings (Table 3). This lava morphology displays small hollow lava tubes left behind by drained lava or hollow flow lobes created by the degassing of the molten lava (Figure 6a) [34]. This morphology is typical of very slow-moving lava causing ponding in the area of hundreds of meters in diameter while the crust consolidates. Successive outflow beneath the crust leads to subsidence, creating the extensively undulating surface and piled up slabs [23,34,74]. Owing to this, the estimated mean surface roughness of shelly pahoehoe in our study area was ~24.93 mm, highest amongst the pahoehoe flows (Table 2). The associated lobes and ripples are visible in the orthomosaic, DTM, and aspect maps given in Figure 6a.

Rubbly aa closely follows shelly pahoehoe in terms of areal extent and location in our region of interest. Rubbly aa is characterized by a clinkery and blocky surface with breccia sizes varying between sand to meters long blocks [34,74] (Figure 7a). In our study area, these morphologies could be observed mainly at the transition of basaltic lava from shelly pahoehoe to aa. This lava morphology is generated after attaining high thermal maturity as a result of which the crust during the flow is broken by brittle failure [34]. Due to these geomorphic processes, the eventual surface displays rough topography; the estimated roughness was ~27.42 mm, nearly double of the spiny pahoehoe flows (Table 2).

Cauliflower aa morphology is marked by irregular outcrops that resemble cauliflowers on the lava surface (Table 2, Figure 7b), typically characterized as smoothly undulating zones with characteristically clinkery surfaces [34]. This lava morphology is usually intermediary during the transformation from pahoehoe to rubbly aa [34]. The protrusions or outcrops are initially attached to the underlying lava, but with time, break and form loose debris [34]. This geomorphic process results in a particularly rough surface and the estimated mean roughness in our region of interest for cauliflower aa was the highest, i.e., ~30.04 mm. However, we identified a region, shown in Figure 7b, where many of these protrusions were intact and attached to the lava flow and provide a fine visual example of cauliflower aa. Cauliflower aa is commonly found in the shelly and slabby pahoehoe-dominated regions where lava flows spilled out after the formation of these morphologies [74] and even in our region of interest, cauliflower aa was found to be closely associated with shelly pahoehoe in the highest elevation zone (Figure 5).

4.2. Cave Opening Distribution and Characterization

The formation of lava tubes and observable cave openings due to collapse in the lava crust is typical of pahoehoe flow morphologies [24]. This was also observed for the present region of interest where the maximum number of small cave openings were reported from the areas of pahoehoe flows; mainly from shelly pahoehoe, followed by spiny pahoehoe flows (Table 3). Shelly pahoehoe flows

were observed in all three elevation classes (Figure 5, Table 3). As explained in the previous section, shelly pahoehoe has extremely tubular morphology with fragile lava crust collapsed at several places making observable small cave openings. The highest elevation zone in our region of interest had the least areal extent but had a significant number of possible small cave openings and thus, highest cave opening density within both, shelly pahoehoe and cauliflower aa flows (Table 3). These openings were hardly of $\sim 1 \text{ m}^2$ of the area on an average (Table 3). The middle elevations had predominance of both, shelly and spiny morphologies and consequently the highest number ($\sim 59\%$ of total) of possible small cave openings with the largest average area of $\sim 1.35 \text{ m}^2$ (Table 3). The lowest elevation class displayed remarkably flat surface with predominantly slabby pahoehoe-type morphology and only 6 possible cave openings out of the total 81 observed (Table 3, Figure 5). The primarily flat topography also resulted in the smallest average area of 0.45 m^2 (Table 3) for the cave openings which could be seen only near the boundary of middle and low elevations (Figure 5).

Table 3. Cave openings in various elevation classes and lava morphologies.

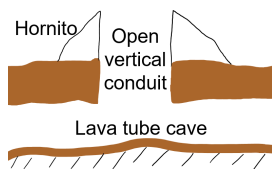
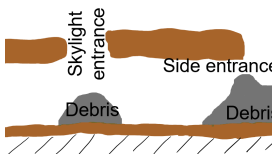
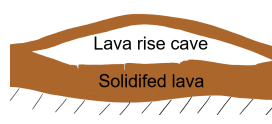
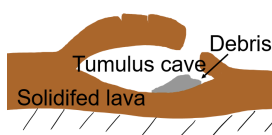
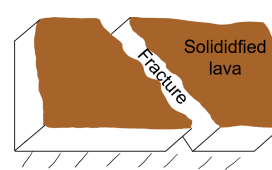
Elevation Class	Elevation Range (m)	Area (km ²)	Number of Caves	Mean Area of Cave Openings (m ²)	Lava Morphology
High	563.92–577.45	0.03	27	1.06	Shelly pahoehoe, Cauliflower aa
Medium	558.26–563.92	0.17	48	1.35	Shelly pahoehoe, Spiny pahoehoe
Low	553.81–558.26	0.13	6	0.45	Slabby pahoehoe, Shelly pahoehoe, Rubbly aa
Total = 81					

The cave density was highest for the high elevation zone (900 km^{-2}), followed by medium ($\sim 282 \text{ km}^{-2}$), and low elevations ($\sim 46 \text{ km}^{-2}$) (Table 3). Gadányi [18,32] mentions that even such small vent cave openings of 1–2 m can widen out towards the bottom reaching up to 4–5 m in the study area. However, the variations in cave frequencies need to be viewed in the light of a possible vent-proximity variable. We suspect that the highest elevation region and the gentle sloping were a result of the thick lava accumulation due to underlying topography and proximity with the fissure vents. On similar shallow slopes in Hawaiian pahoehoe flow fields, Walker [78] also reported that tumuli and lava rises covered a substantial proportion, exceeding 50%, of the total area. Based on the pre-flow topography, Rossi [34] confirms the presence of considerable topographic depressions at several places with the average lava flow thickness reaching up to 11 m. In our study site, the average elevation rise from low-to-medium and medium-to-high elevations reaches up to $\sim 10 \text{ m}$ and explains the high cave density due to underlying hollowness or depressions.

We observed mainly five types of possible cave openings in the study area (Table 4). In the mapped area, open vertical conduits and collapsed lava tunnels were predominantly observed. This, however, does not necessarily indicate that the small tumulus caves and lava rise caves would be less prevalent in similar lava flows, as the openings of hidden or tumulus caves and lava rise caves are lateral and difficult to observe in down-looking aerial photos. Therefore, the oblique (20°) UAV survey as performed by us, coupled with 3D perspective views can be useful in identifying such openings. Table 4 provides the morphological descriptions of these caves along with relevant references. Gadányi [18] has provided detailed discussions on such caves in Iceland. In Figure 8, we display these small caves through field photographs, aerial photographs, and DTMs. For open vertical conduits (Figure 8a), a distinct locally elevated vent terrain is visible as oval or round shaped vertical passageways, where lava rose to the surface and then waned. Collapsed lava tunnels are identifiable as the locally elevated channels in the high-resolution DTM in Figure 8b. The visible holes in the collapsed roof are often referred to as “Skylights”. While on Mars, skylights of tens to more than 100 m diameters have been reported, in our study area, using the high-resolution imaging, we characterize skylights of even 1–2 m diameters. Tumulus lava caves (Figure 8c) are rightly called “Hidden” caves as they are hard to detect remotely. However, the high-resolution DTM that we generated marks a contour around the elevated

opening of such caves (Figure 8c). Such caves are formed due to the collapse of the unstable section of the crust formed due to the bulging and solidification of injected lava. These cave openings can also be as small as a few centimeters to a meter. Lava rise cave (Figure 8d) was another type of caves in the study area that was tough to spot in the aerial images. Due to the largely flat topography and their lateral openings, even the high-resolution DTM of these caves did not show any significantly marked elevation rise (Figure 8d). The 3D perspective views proved to be useful for identifying such openings. Figure 8e shows small surface fractures in the form of open cracks formed due to tensile stress in lava during and after solidification. The elongated terrain of one of such fractures can be observed in the DTM shown in Figure 8e. Although there are large fractures in the Leirhnjúkur lava field [81], the average width of the small surface fractures reported here are ≤ 1 m. Based on aerial photography, Opheim and Gudmundsson [81] characterized more than a thousand of fractures with exceptionally high width-to-length ratios (1:20 to 1:40) in this lava field. These previously reported fractures [81] were an order of magnitude larger than the ones we report here using cm-resolution UAV images. However, the width-to-length ratio for these smaller fractures is still the same as reported by Opheim and Gudmundsson [81]. The majority of these fractures end bluntly as tectonic caves [81]. To further confirm our findings, it is worth mentioning here that similar centimeter-scale fractures have also been reported by Müller et al. [71] in the Holuhraun fissure eruption site, Iceland, using UAV images and photogrammetry.

Table 4. Description of types of possible small cave openings observed in the study area.

Type	Description	Sketch	Reference
Open vertical conduit	These structures have oval or round shaped vertical passageways and are found in recent volcanic rocks, where lava rose to the surface and then waned. The openings are typically marked by a rootless small spatter cone called hornito.		[18,66]
Collapsed lava tunnel (Skylights)	Skylights are openings where the roof of the lava tube has collapsed. In an active flow, these skylights allow convective cooling of the lava.		[79,80]
Lava rise cave	Lava rise caves are formed as a result of inflation due to fluid lava accumulating under the solidified surface crust. Once the lava drains leaving a deflated center, if the uplifted surface crust can support itself, a flat cave remains under it.		[18]
Hidden or tumulus cave	Tumulus lava caves are formed when during volcanic activity below the arching surface crust, liquid lava is injected causing the surface crust to bulge as it solidifies without any horizontal shortening. Once the lava drains, the unstable section of the crust collapses revealing the tumulus cave.		[18]
Surface fractures	The observed small surface fractures are deep open cracks that are formed due to tensile stress in lava during and after solidification.		[71,81]

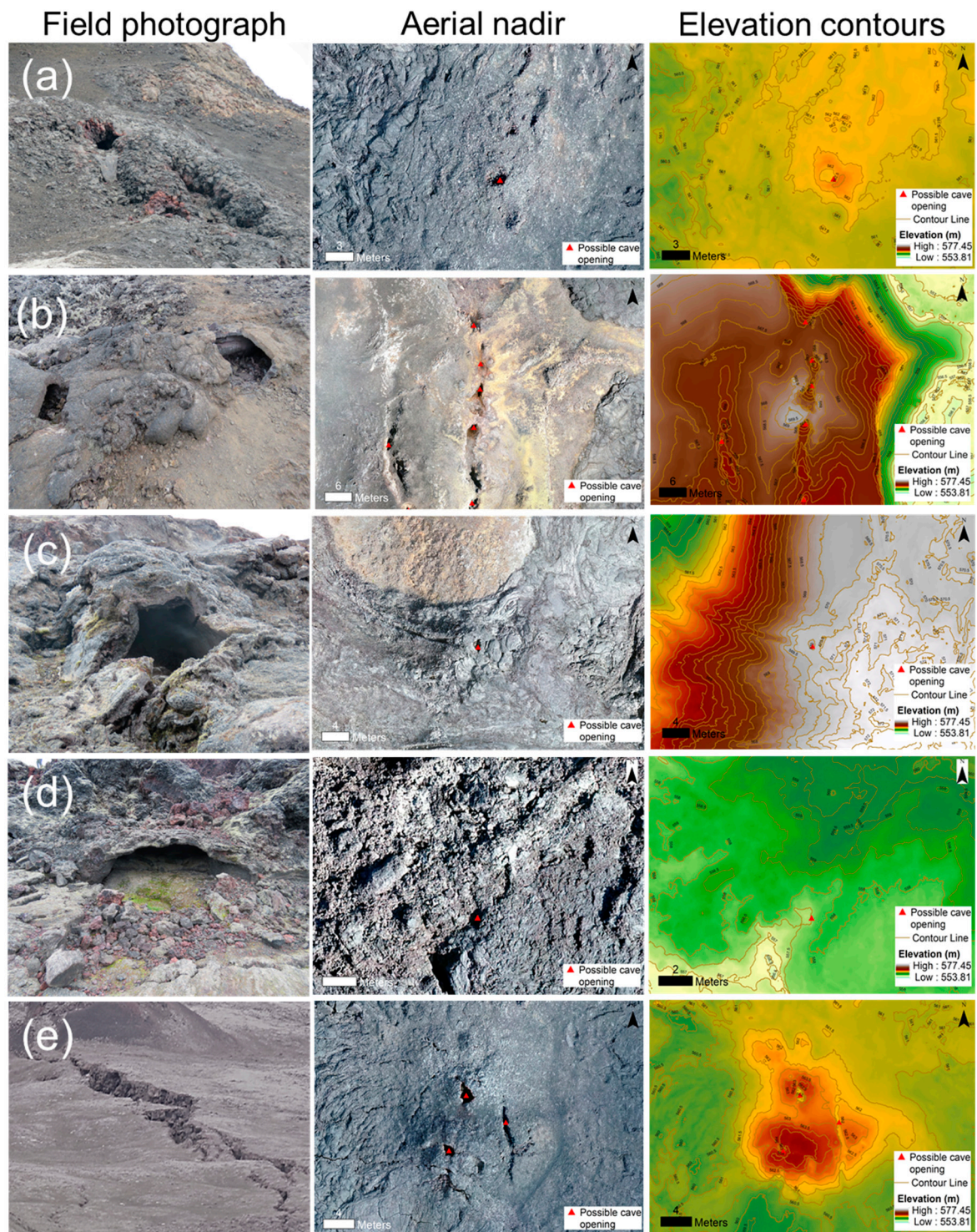


Figure 8. Types of possible small cave openings observed in the study area: (a) open vertical conduit; (b) collapsed small lava tunnel; (c) tumulus cave; (d) lava rise cave; (e) surface fractures. All the zoomed-in elevation maps are presented with respect to a common elevation scale to enable observing relative elevations and topography possible for each cave type.

4.3. Possible Analogies with Martian lava flows

Before discussing any such analogy, there are several important points to consider. First, the topographical details of the lava flow on Mars are largely obscured by dust and make any meter-

or submeter-scale morphological observations difficult. Only, the broad flow morphologies such as braided lava channels, fan-shaped lobes, and the extent of terrain roughness provide some clues on the possible characterization of Martian lava flows [82]. Second, identifying possible small cave entrances in Martian images is a very challenging task due to the unavailability of submeter resolution High Resolution Imaging Science Experiment (HiRISE) images for a vast majority of the Martian terrain. A recent database led by Glen Cushing of U.S. Geological Survey [83] and called Mars Global Cave Candidate Catalog (MGC³) [84] is an exciting start. Figure 9 shows the global distribution of sighted possible caves on Mars based on MGC³. This database is based on the images from the Mars Reconnaissance Orbiter's (MRO's) Context Camera (CTX) and HiRISE camera. While CTX images have best of the resolutions of ~5–6 m/pixel and can resolve a possible cave entrance candidate of ~20–25 m diameter, the presence of HiRISE images of some of such candidates can provide more clues, i.e., cliff-wall strata, underlying aeolian bedforms, and dust/bedrock interfaces, at ~0.25 m/pixel resolutions. Third, none of these cave candidates can be verified as actual caves with sufficient subsurface void spaces until they are physically visited. However, as mentioned in the beginning, even smaller caves with up to several meters to tens of meters of sheltered space can have significant astrobiological significance. Therefore, in this section, we provide certain examples of possible small pit craters/caves on Mars which can be comparable to the small cave entrances which we report for the Icelandic lava flow. Considering the lower gravity of Mars that can allow equivalents of such smaller terrestrial caves to be up to an order of magnitude larger on Mars, such caves can be interesting targets for future Mars exploration.

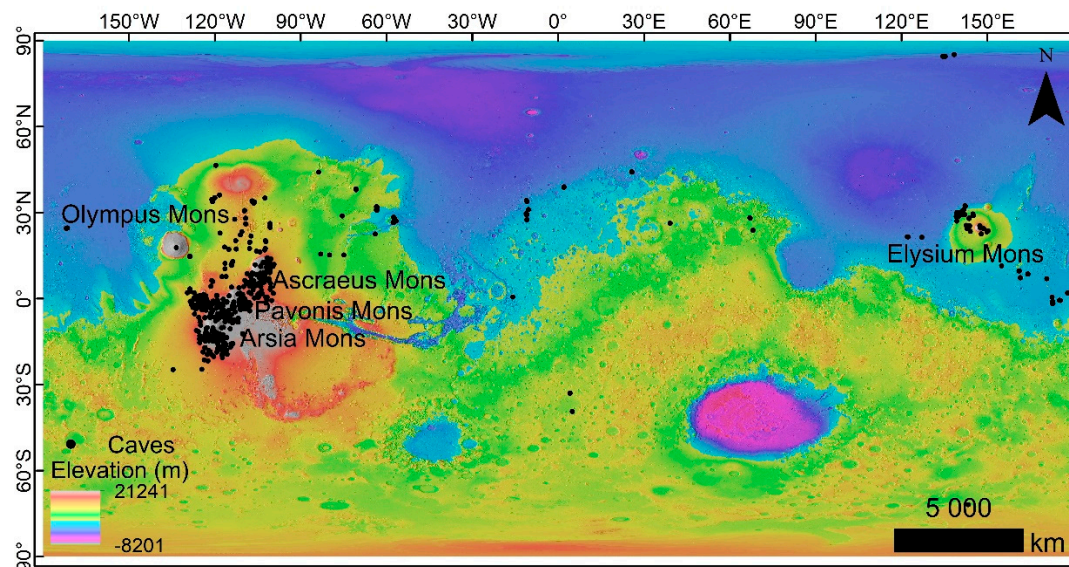


Figure 9. Global distribution of sighted possible caves on Mars. Mars Orbiter Laser Altimeter (MOLA) elevation and hillshaded view is in the background (courtesy: NASA/JPL/Goddard). The cave locations are retrieved from Mars Global Cave Candidate Catalog (MGC³) [84].

Figure 9 marks the Tharsis region on Mars as the hotspot of possible caves. Tharsis is home to the largest volcanoes in the Solar System forming a vast volcanic plateau centered around the equator in the western hemisphere of Mars. The three enormous shield volcanoes Arsia Mons, Pavonis Mons, and Asraeus Mons, which are collectively known as the Tharsis Montes, also provide interesting geomorphological variabilities at the intersections of their lava fields. A closer look at the topographical characteristics of the lava fields and the corresponding presence of possible caves derived from MGC³ reveals that such caves are predominantly present in the smooth-textured pahoehoe-type lava flows. The extensive presence of collapsed or semi-intact lava channels/tubes in this region [82] suggests the prevalence of a possible shelly pahoehoe-type morphology; extremely vesicular [82] with fragile lava crust and therefore consisting of observable small cave openings. This morphology is characteristic of

sluggish lava causing ponding in a vast area while the crust consolidates and the successive outflow beneath the crust leads to subsidence, creating the possibility of pit cratering and extensively undulating surface. Thus, what we observe as possible skylights or cave openings in this region are primarily pit craters. Cushing [85] has detailed on the morphology of such huge pit craters and possible caves in this region. Crown and Ramsey [82] have discussed aa and pahoehoe-type morphologies of lava flows in the Tharsis region where low-viscosity flows were predominantly transported through channels/tubes, inflating in vast plains. An example of this can be seen in Figure 10 where we present a well-studied pit crater [85] in a pahoehoe-type smooth textured flow, adjacent to the rough-textured aa-type flow in the lava field of Pavonis Mons (Figure 10a). The HiRISE image (Figure 10b) and DTM (Figure 10c) additionally highlight this subsidence feature consisting of a subterranean void and a debris pile in the center, ~30 m further down the central cave opening. The diameter of the central collapse is ~41.5 m while that of the overall subsidence feature is ~188 m. However, while this is an example of relatively huge subsidence in a distinctly demarcated pahoehoe-type flow, in the following examples from the Tharsis region, we try to highlight several of the smaller possible cave openings which are dimensionally closer to our terrestrial analogs.

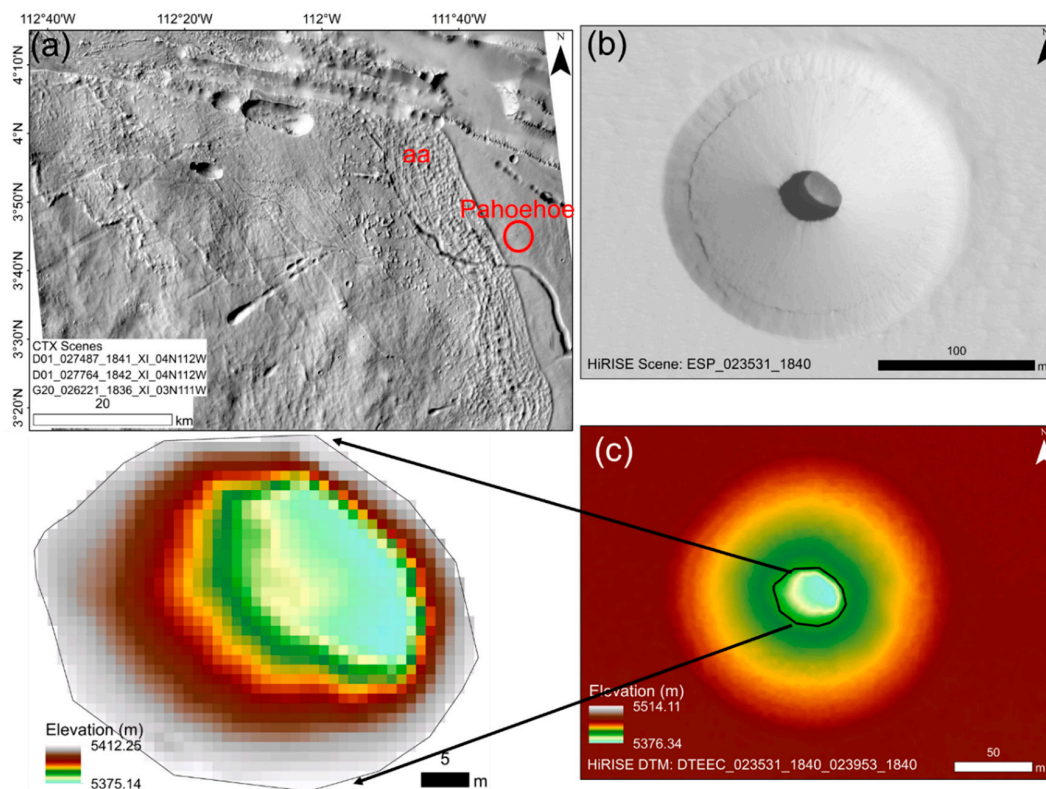


Figure 10. A huge pit crater in the lava field of Pavonis Mons: (a) contextual map generated using CTX mosaic and showing the cave location along with the lava flow morphologies and channels; (b) HiRISE view of the cave opening; (c) HiRISE DTM showing elevation changes in and around the cave opening. The image IDs are provided within the maps. CTX image credit: NASA/JPL-Caltech. HiRISE image credit: NASA/JPL/University of Arizona.

Figures 11–13 show that the visible lava channels are one of the best targets to search for such cave openings. Cushing et al. [83] called a morphological group of such subsidence structures “Atypical Pit Craters (APCs)”. APCs usually have sharp and definite rims with surface diameters of ~50–350 m [83]. However, in the subsequent examples, we will discuss some smaller APCs too. In Figure 11a, we observe a collapsed skylight north of Arsia Mons with a possible subterranean hollow space (marked by black dotted lines). The different texture within the black dotted lines suggests a slightly elevated and sloped terrain that allows for a changed dust pattern than the surrounding terrain. The diameter

of this opening is ~90 m. The small pit crater shown in Figure 11b in an otherwise intact lava tube was sighted on the Asraeus Mons summit region. This APC was particularly interesting due to its smaller than usual diameter of ~23 m and its presence on a seemingly intact lava tube.

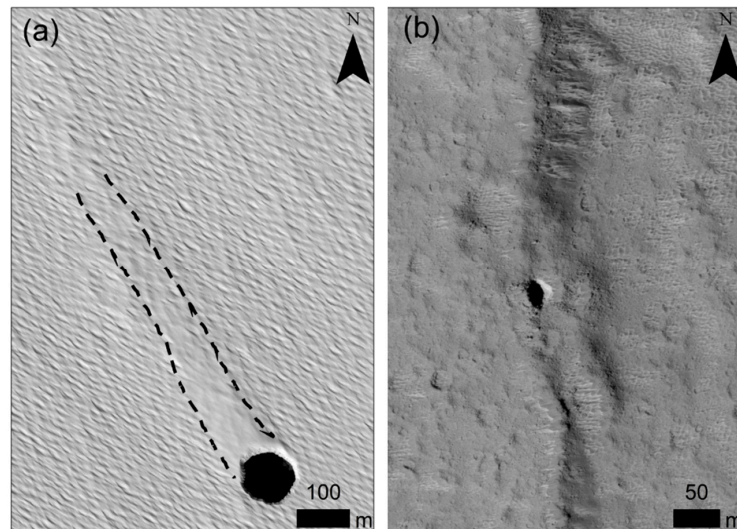


Figure 11. HiRISE view of pit craters of different dimensions: (a) a collapsed skylight with a possible subterranean hollow space (marked by black dotted lines) evident due to the textural differences (Scene ID: ESP_013167_1785); (b) a small pit crater in an otherwise intact lava tube (Scene ID: ESP_012863_1915). HiRISE image credit: NASA/JPL/University of Arizona.

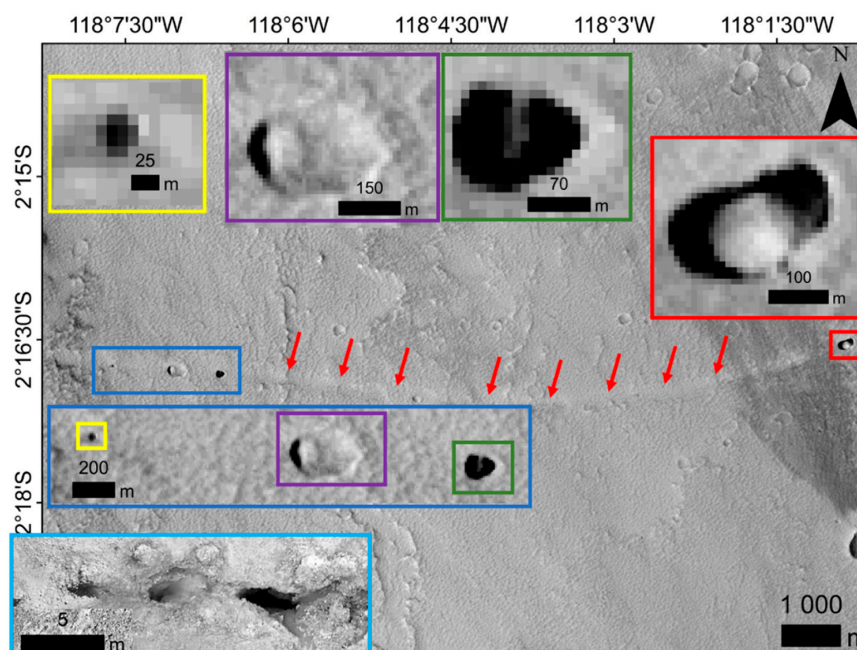


Figure 12. Multiple pit craters in the same lava channel (marked by red arrows) displaying various morphologies and dimensions (CTX Scene ID: J14_050313_1778_XI_02S118W). The red rectangle shows a pit crater with a visible mound in the middle. The blue rectangle highlights three craters separated by several kilometers. The subsidence structure within the green rectangle is a seemingly hollow pit crater, the one within the violet rectangle is the largest of the three but filled with debris, and the smallest of these structures is marked by the yellow rectangle. The inset figure within the cyan rectangle shows an analogous chain of small cave openings in our Icelandic study area. CTX image credit: NASA/JPL-Caltech.

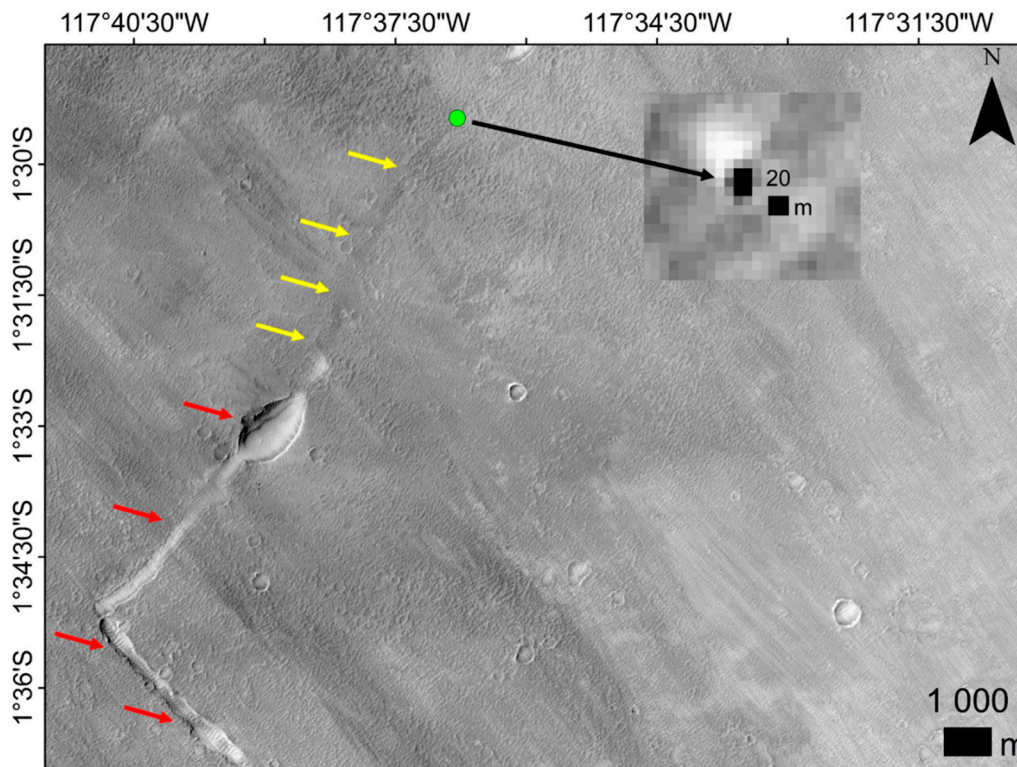


Figure 13. A possible small subsidence cave opening in a lava tube (CTX Scene ID: G18_025285_1769_XN_03S117W). The red arrows mark the collapsed part of the lava tube and a possible fissure while the yellow arrows mark the intact part. The green dot marks the possible cave opening that can be seen in the zoomed-in version indicated by the black arrow. CTX image credit: NASA/JPL-Caltech.

Figure 12 highlights multiple APCs within the same lava channel. These APCs display remarkably different morphologies and dimensions. For example, the red rectangle marks a pit crater with shadows surrounding the middle portion, suggesting it to be a visible mound of accumulated debris and dust (Figure 12). The blue rectangle emphasizes three craters separated by several kilometers: (1) the APC within the green rectangle is a seemingly hollow pit crater with the indiscernible floor, (2) the APC within the violet rectangle is the largest of the three APCs and is filled with debris, and (3) the smallest of these APCs marked by the yellow rectangle is only ~27 m in diameter. This small cave within the yellow rectangle is not yet listed in the MGC³, and here we are reporting it as a representative of more of such small caves which are hard to observe in presently available satellite images. The availability of HiRISE images for the smallest crater might have provided better insights. In Figure 12, we also provide an inset figure within the cyan rectangle that shows an analogous chain of small cave openings in a small lava channel in our Icelandic study area. However, the scale of these observations should be noted with care. As expected, the dimensions of the Icelandic APCs are more than an order of magnitude smaller than the Martian APCs. The rightmost APC in the inset image shows a deeper hollow pit, the middle one is largely filled with debris, and the leftmost is the smallest one with hardly 1 m of diameter. In Figure 13, we show another possible APC with a remarkably small diameter of ~20 m. This small APC is again, not yet listed within the MGC³, and here we identify and report it. Identifying such APCs on CTX images is difficult and the availability of a HiRISE image would have been ideal. However, with the contextual interpretations such as the one highlighted in Figure 13, these possible APCs can be marked with an acceptable level of confidence. The red arrows in Figure 13 show the collapsed part of a huge lava tube and associated fissure while the yellow arrows mark the intact part. This supports the possibility of the observed dark albedo feature marked by the green dot and shown in the zoomed-in inset image to be an APC.

5. Conclusions

We investigated a part of an Icelandic lava flow as a Mars analog environment, by performing a dedicated remote-sensing-based characterization of possible small-cave openings in Leirhnjúkur fissure volcano lava fields. One might argue that probably the Hawaiian lava fields would have been a better analog as those are bigger than the Leirhnjúkur fissure volcano lava fields and are also closer to the shield volcanoes like the ones in Tharsis on Mars. However, for investigating the small lava cave environment that was the focus of our study, an analog site such as the Leirhnjúkur fissure volcano lava fields seemed appropriate because this region has a similar kind of rigorous aeolian-volcanic interactions as on Mars. The fissure nature of eruptions in this region provides the possibility of lower lava volume and subsequently smaller tubes, channels, caves, and folds. Furthermore, sites of possible fissure eruptions, like the one we have selected in Iceland, have also been reported in the Tharsis region on Mars [86,87]. Our analog study is even more relevant considering a recent paper [40] which suggests that the possible mudflows on Mars might have propagated like the terrestrial pahoehoe lava flows and show similar morphological characteristics. Figure 2d of Broz et al. [40] shows the presence of extensive voids or cavities within the simulated mudflow under Martian conditions. These cavities appear to be of smaller scale than the usual caves within a pahoehoe lava flow. This signifies the premise of our research that while the presence of small caves in pahoehoe-type flows on Mars is elusive due to the resolution limitations of the present remote sensors, such caves might be abundant on Mars with considerable significance for astrobiology or habitability.

The study by Favalli et al. [22] has already emphasized the importance of UAV imaging and terrain data in resolving lava surfaces and enabling identification of folds and small openings. The fact that we could characterize 81 small cave openings/folds of $<1.5\text{ m}^2$ average area, within a small section of the lava flow, is the proof that fine resolution datasets can be extremely useful in furthering our understanding of these landforms. We observed that the existence of such small cave openings is favored in the regions which show vesicular lava crust flow morphology. By analogy, we performed a visual analysis of similar shelly pahoehoe-type lava flows in the Tharsis region of Mars using available best resolution satellite images. In analogy to its terrestrial counterpart, this region on Mars shows the potential existence of small cave openings that have diameters as small as $\sim 20\text{ m}$.

The smaller ($\sim 20\text{ m}$) cave openings which we have identified in CTX images support our hypothesis that such small caves, analogous to small Icelandic caves but an order of magnitude larger than them, might be in abundance on Mars. The unavailability of submeter resolution images for $\sim 95\%$ of the Martian terrain makes it impossible to characterize any such cave opening that is lesser than $\sim 20\text{--}25\text{ m}$ in diameter. Nevertheless, the astrobiological and ISRU significance of such small caves is irrefutable. Future targeted HiRISE acquisitions of such possible cave openings from multiple view angles will not only confirm their existence but will also provide important terrain and morphological details for planning future missions. Until now, APCs seem to be the prevalent volcanic cave type on Mars but with future availability of more HiRISE images covering new regions, more small cave types analogous to the terrestrial ones as shown in Figure 8 can be observed.

The importance of having thermal infrared observations in confirming caves is well-established [85,88] but the presently operational thermal sensors around Mars do not have sufficient spatial resolutions to confirm the meter-scale cave openings. Future orbiter, rover, and even UAV missions for Mars should try accommodating high-resolution thermal sensors as payloads. The next phase of our research is going to cover the same region in Iceland in the thermal infrared range during day and night to observe the thermal characteristics of these small caves. If a future rover mission targets volcanic sites, even sending a Ground Penetrating Radar (GPR) can be useful in finding the possibilities of subsurface hollowness around such subsidence structures.

Another plausible continuation of this research can focus on taking field measurements of morphometrics and diurnal environmental conditions (mainly temperature, relative humidity, and degree of insolation) within such small caves to enable numerical modeling of analogous structures on Mars. The possibility that such small cave openings can lead to vast subterranean hollow spaces

cannot be ruled out on Mars considering its lower gravity and the ongoing Mars cave research needs to reconsider the possibility and significance of the small Martian caves given our results.

Author Contributions: Conceptualization, L.S. and A.B.; field data collection, A.B. and J.A.R.L.; data processing, L.S., A.B., and J.A.R.L.; formal analysis, L.S., A.B.; investigation, L.S., A.B., and S.S.; methodology, L.S. and A.B.; software, L.S. and A.B.; writing—original draft, L.S.; funding acquisition, F.J.M.-T. and M.-P.Z., writing—review and editing, A.B., S.S., F.J.M.-T., and M.-P.Z. All authors have read and agreed to the published version of the manuscript.

Funding: This research received no external funding.

Acknowledgments: We thank the efforts of the handling editor Prof. Ulrich Kamp and the reviewers for their suggestions in improving the paper. We acknowledge the Wallenberg Foundation and the Kempe Foundation for supporting our Mars research activities in general. M.-P.Z. has been partially funded by the Spanish State Research Agency (AEI) Project No. MDM-2017-0737 Unidad de Excelencia “María de Maeztu”- Centro de Astrobiología (INTA-CSIC). We thank NASA, JPL, and the University of Arizona for providing HiRISE images free of charge. The maps in various figures have been created using ArcGIS version 10.6.1. ArcticDEM is provided by the Polar Geospatial Center under NSF-OPP awards 1043681, 1559691, and 1542736.

Conflicts of Interest: The authors declare no conflicts of interest. The funders had no role in the design of the study; in the collection, analyses, or interpretation of data; in the writing of the manuscript, or in the decision to publish the results.

References

1. Rummel, J.D.; Beaty, D.W.; Jones, M.A.; Bakermans, C.; Barlow, N.G.; Boston, P.J.; Chevrier, V.F.; Clark, B.C.; de Vera, J.-P.P.; Gough, R.V.; et al. A new analysis of Mars “Special Regions”: Findings of the second MEPAG Special Regions Science Analysis Group (SR-SAG2). *Astrobiology* **2014**, *14*, 887–968. [[CrossRef](#)]
2. Sam, L.; Bhardwaj, A.; Singh, S.; Martin-Torres, F.J. UAV Imaging of Small Caves in Icelandic Lava Field as Possible Mars Analogues. In Proceedings of the 3rd International Planetary Caves Conference, San Antonio, TX, USA, 18–21 February 2020.
3. Martin-Torres, J.; Olsson, P.; Zorzano, M.P.; Bhardwaj, A.; Sam, L.; Singh, S. Martian Caves as Special Region Candidates. In Proceedings of the 3rd International Planetary Caves Conference, San Antonio, TX, USA, 18–21 February 2020.
4. Boston, P.J.; Spilde, M.N.; Northup, D.E.; Melim, L.A.; Soroka, D.S.; Kleina, L.G.; Lavoie, K.H.; Hose, L.D.; Mallory, L.M.; Dahm, C.N.; et al. Cave Biosignature Suites: Microbes, Minerals, and Mars. *Astrobiology* **2001**, *1*, 25–55. [[CrossRef](#)]
5. Léveillé, R.J.; Datta, S. Lava tubes and basaltic caves as astrobiological targets on Earth and Mars: A review. *Planet. Space Sci.* **2010**, *58*, 592–598. [[CrossRef](#)]
6. Northup, D.E.; Melim, L.A.; Spilde, M.N.; Hathaway, J.J.M.; Garcia, M.G.; Moya, M.; Stone, F.D.; Boston, P.J.; Dapkevicus, M.L.N.E.; Riquelme, C. Lava cave microbial communities within mats and secondary mineral deposits: Implications for life detection on other planets. *Astrobiology* **2011**, *11*, 601–618. [[CrossRef](#)]
7. Popa, R.; Smith, A.R.; Popa, R.; Boone, J.; Fisk, M. Olivine-respiring bacteria isolated from the rock-ice interface in a lava-tube cave, a Mars analog environment. *Astrobiology* **2012**, *12*, 9–18. [[CrossRef](#)] [[PubMed](#)]
8. Stamenković, V.; Beegle, L.W.; Zacny, K.; Arumugam, D.D.; Baglioni, P.; Barba, N.; Baross, J.; Bell, M.S.; Bhartia, R.; Blank, J.G.; et al. The next frontier for planetary and human exploration. *Nat. Astron.* **2019**, *3*, 116–120. [[CrossRef](#)]
9. Boston, P.J.; Frederick, R.D.; Welch, S.M.; Werker, J.; Meyer, T.R.; Sprungman, B.; Hildreth-Werker, V.; Thompson, S.L.; Murphy, D.L. Human utilization of subsurface extraterrestrial environments. *Gravit. Space Biol. Bull.* **2003**, *16*, 121–131. [[PubMed](#)]
10. Horz, F. *Lava Tubes—Potential Shelters for Habitats*; Lunar bases and space activities of the 21st century; Lunar and Planetary Institute: Houston, TX, USA, 1985.
11. Frederick, R.D.; Billings, T.L.; McGown, R.D.; Walden, B.E. *Martian Ice Caves*; Workshop on Concepts and Approaches for Mars Exploration, 18–20 July 2000; Lunar and Planetary Institute: Houston, TX, USA, 2000; Abstract number 6062; pp. 114–115.
12. Williams, K.E.; McKay, C.P.; Toon, O.B.; Head, J.W. Do ice caves exist on Mars? *Icarus* **2010**, *209*, 358–368. [[CrossRef](#)]

13. Daga, A.W.; Battler, M.M.; Burke, J.D.; Crawford, I.A.; L veill , R.J.; Simon, S.B.; Tan, L.T. Lunar and Martian Lava Tube Exploration as Part of an Overall Scientific Survey. In Proceedings of the NASA Solar System Exploration, Annual Meeting of the Lunar Exploration Analysis Group, Houston, TX, USA, 16–19 November 2009.
14. Common Questions about InSight’s “Mole”. Available online: <https://mars.nasa.gov/news/8444/common-questions-about-insights-mole?site=insight> (accessed on 5 July 2019).
15. Wasilewski, T.G. Evaluation of drilling-based water extraction methods for Martian ISRU from mid-latitude ice resources. *Planet. Space Sci.* **2018**, *158*, 16–24. [[CrossRef](#)]
16. Cave Skylights Spotted on Mars|Science Mission Directorate. Available online: https://science.nasa.gov/science-news/science-at-nasa/2007/21sep_caves (accessed on 5 July 2019).
17. Caves Spotted on Mars. Available online: <http://www.nature.com/articles/news070312-11> (accessed on 5 July 2019).
18. Gad nyi, P. Caves Under Uplifted Surface Crusts of Basalt Lava Flows. In Proceedings of the 10th International Symposium on Pseudokarst, Gorizia, Italy, 29 April–2 May 2008; pp. 119–126.
19. Calvari, S.; Pinkerton, H. Formation of lava tubes and extensive flow field during the 1991–1993 eruption of Mount Etna. *J. Geophys. Res. Solid Earth* **1998**, *103*, 27291–27301. [[CrossRef](#)]
20. Calvari, S.; Pinkerton, H. Lava tube morphology on Etna and evidence for lava flow emplacement mechanisms. *J. Volcanol. Geotherm. Res.* **1999**, *90*, 263–280. [[CrossRef](#)]
21. Duncan, A.M.; Guest, J.E.; Stofan, E.R.; Anderson, S.W.; Pinkerton, H.; Calvari, S. Development of tumuli in the medial portion of the 1983 aa flow-field, Mount Etna, Sicily. *J. Volcanol. Geotherm. Res.* **2004**, *132*, 173–187. [[CrossRef](#)]
22. Favalli, M.; Fornaciai, A.; Nannipieri, L.; Harris, A.; Calvari, S.; Lormand, C. UAV-based remote sensing surveys of lava flow fields: A case study from Etna’s 1974 channel-fed lava flows. *Bull. Volcanol.* **2018**, *80*, 29. [[CrossRef](#)]
23. Hon, K.; Kauahikaua, J.; Denlinger, R.; Mackay, K. Emplacement and inflation of pahoehoe sheet flows: Observations and measurements of active lava flows on Kilauea Volcano, Hawaii. *Geol Soc Am Bull.* **1994**, *106*, 351–370. [[CrossRef](#)]
24. Peterson, D.W.; Holcomb, R.T.; Tilling, R.I.; Christiansen, R.L. Development of lava tubes in the light of observations at Mauna Ulu, Kilauea Volcano, Hawaii. *Bull. Volcanol.* **1994**, *56*, 343–360. [[CrossRef](#)]
25. Kauahikaua, J.; Cashman, K.V.; Mattox, T.N.; Heliker, C.C.; Hon, K.A.; Mangan, M.T.; Thornber, C.R. Observations on basaltic lava streams in tubes from Kilauea Volcano, island of Hawai’i. *J. Geophys. Res. Solid Earth* **1998**, *103*, 27303–27323. [[CrossRef](#)]
26. Orr, T.R.; Bleacher, J.E.; Patrick, M.R.; Wooten, K.M. A sinuous tumulus over an active lava tube at Kilauea Volcano: Evolution, analogs, and hazard forecasts. *J. Volcanol. Geotherm. Res.* **2015**, *291*, 35–48. [[CrossRef](#)]
27. McLaughlin, D.B. Volcanism and aeolian deposition on Mars. *Gsa Bull.* **1954**, *65*, 715–718. [[CrossRef](#)]
28. McLaughlin, D.B. The volcanic-aeolian hypothesis of Martian features. *Publ. Astron. Soc. Pac.* **1956**, *68*, 211–218. [[CrossRef](#)]
29. Edgett, K.S.; Lancaster, N. Volcaniclastic aeolian dunes: Terrestrial examples and application to Martian sands. *J. Arid Environ.* **1993**, *25*, 271–297. [[CrossRef](#)]
30. Edgett, K.S. Aeolian dunes as evidence for explosive volcanism in the Tharsis region of Mars. *Icarus* **1997**, *130*, 96–114. [[CrossRef](#)]
31. Arnalds, O.; Dagsson-Waldhauserova, P.; Olafsson, H. The Icelandic volcanic aeolian environment: Processes and impacts—A review. *Aeolian Res.* **2016**, *20*, 176–195. [[CrossRef](#)]
32. Gad nyi, P. Formation, Types and Morphology of Basalt Lava Caves. Ph.D. Thesis, University of P cs, Faculty of Natural Sciences Doctoral School of Earth Sciences, P cs, Hungary, 2010.
33. Hr arsson, B.; J nsson, S.S. Lava Caves in the Hallmundarhraun Lava Flow, Western Iceland. In Proceedings of the 6th International Symposium on Vulcanospeleology, Hilo, HI, USA, 5–9 August 1991; pp. 85–88.
34. Rossi, M.J. Morphology of the 1984 open-channel lava flow at Krafla volcano, northern Iceland. *Geomorphology* **1997**, *20*, 95–112. [[CrossRef](#)]
35. Bhardwaj, A.; Sam, L.; Akanksha; Mart n-Torres, F.J.; Kumar, R. UAVs as remote sensing platform in glaciology: Present applications and future prospects. *Remote Sens. Environ.* **2016**, *175*, 196–204. [[CrossRef](#)]
36. Gaffey, C.; Bhardwaj, A. Applications of Unmanned Aerial Vehicles in Cryosphere: Latest Advances and Prospects. *Remote Sens.* **2020**, *12*, 948. [[CrossRef](#)]

37. Mars Helicopter to Fly on NASA's Next Red Planet Rover Mission. Available online: <http://www.nasa.gov/press-release/mars-helicopter-to-fly-on-nasa-s-next-red-planet-rover-mission> (accessed on 5 July 2019).
38. Nakano, T.; Kamiya, I.; Tobita, M.; Iwahashi, J.; Nakajima, H. Landform monitoring in active volcano by UAV and SfM-MVS technique. *ISPRS Int. Arch. Photogramm. Remote Sens. Spat. Inf. Sci.* **2014**, *XL–8*, 71–75. [[CrossRef](#)]
39. Turner, N.R.; Perroy, R.L.; Hon, K. Lava flow hazard prediction and monitoring with UAS: A case study from the 2014–2015 Pāhoā lava flow crisis, Hawai'i. *J. Appl. Volcanol.* **2017**, *6*, 17. [[CrossRef](#)]
40. Brož, P.; Krýza, O.; Wilson, L.; Conway, S.J.; Hauber, E.; Mazzini, A.; Raack, J.; Balme, M.R.; Sylvest, M.E.; Patel, M.R. Experimental evidence for lava-like mud flows under Martian surface conditions. *Nat. Geosci.* **2020**. [[CrossRef](#)]
41. Hjartardóttir, Á.R.; Einarsson, P.; Bramham, E.; Wright, T.J. The Krafla fissure swarm, Iceland, and its formation by rifting events. *Bull. Volcanol.* **2012**, *74*, 2139–2153. [[CrossRef](#)]
42. Aufaristama, M.; Höskuldsson, A.; Jónsdóttir, I.; Ólafsdóttir, R. Mapping and Assessing Surface Morphology of Holocene Lava Field in Krafla (NE Iceland) Using Hyperspectral Remote Sensing. In Proceedings of the IOP Conference Series: Earth and Environmental Science; IOP Publishing Ltd.: Bristol, UK, 2016; Volume 29, p. 012002. [[CrossRef](#)]
43. Bhardwaj, A.; Sam, L.; Martín-Torres, F.J.; Zorzano, M.-P.; Ramírez Luque, J.A. UAV imaging of a Martian brine analogue environment in a fluvio-aeolian setting. *Remote Sens.* **2019**, *11*, 2104. [[CrossRef](#)]
44. Ullman, S. The interpretation of structure from motion. *Proc. R. Soc. Lond. B Biol. Sci.* **1979**, *203*, 405–426. [[CrossRef](#)]
45. Manfreda, S.; Dvorak, P.; Mullerova, J.; Herban, S.; Vuono, P.; Arranz Justel, J.J.; Perks, M. Assessing the accuracy of Digital Surface Models derived from optical imagery acquired with Unmanned Aerial Systems. *Drones* **2019**, *3*, 15. [[CrossRef](#)]
46. James, M.R.; Robson, S. Mitigating systematic error in topographic models derived from UAV and ground-based image networks. *Earth Surf. Process. Landf.* **2014**, *39*, 1413–1420. [[CrossRef](#)]
47. Wackrow, R.; Chandler, J.H. Minimising systematic error surfaces in digital elevation models using oblique convergent imagery. *Photogramm. Rec.* **2011**, *26*, 16–31. [[CrossRef](#)]
48. Sona, G.; Pinto, L.; Pagliari, D.; Passoni, D.; Gini, R. Experimental analysis of different software packages for orientation and digital surface modelling from UAV images. *Earth Sci. Inf.* **2014**, *7*, 97–107. [[CrossRef](#)]
49. Burns, J.H.R.; Delparte, D.; Gates, R.D.; Takabayashi, M. Integrating structure-from-motion photogrammetry with geospatial software as a novel technique for quantifying 3D ecological characteristics of coral reefs. *Peer J.* **2015**, *3*, e1077. [[CrossRef](#)]
50. Iizuka, K.; Itoh, M.; Shiodera, S.; Matsubara, T.; Dohar, M.; Watanabe, K. Advantages of unmanned aerial vehicle (UAV) photogrammetry for landscape analysis compared with satellite data: A case study of postmining sites in Indonesia. *Cogent Geosci.* **2018**, *4*, 1498180. [[CrossRef](#)]
51. Kersten, T.P.; Lindstaedt, M. Image-Based Low-Cost Systems for Automatic 3D Recording and Modelling of Archaeological Finds and Objects. In *Proceedings of the Progress in Cultural Heritage Preservation*; Ioannides, M., Fritsch, D., Leissner, J., Davies, R., Remondino, F., Caffo, R., Eds.; Springer: Berlin/Heidelberg, Germany, 2012; pp. 1–10.
52. Themistocleous, K.; Ioannides, M.; Agapiou, A.; Hadjimitsis, D.G. The Methodology of Documenting Cultural Heritage Sites Using Photogrammetry, UAV, and 3D Printing Techniques: The Case Study of Asinou Church in Cyprus. In *Proceedings of the Third International Conference on Remote Sensing and Geoinformation of the Environment (RSCy2015)*; International Society for Optics and Photonics: Paphos, Cyprus, 2015; Volume 9535, p. 953510. [[CrossRef](#)]
53. Verhoeven, G. Taking computer vision aloft—archaeological three-dimensional reconstructions from aerial photographs with photostan. *Archaeol. Prospect.* **2011**, *18*, 67–73. [[CrossRef](#)]
54. Furukawa, Y.; Ponce, J. Accurate Camera Calibration from Multi-View Stereo and Bundle Adjustment. *Int. J. Comput. Vis.* **2009**, *84*, 257–268. [[CrossRef](#)]
55. Dirscherl, M.; Rossi, C. Geomorphometric analysis of the 2014–2015 Bárðarbunga volcanic eruption, Iceland. *Remote Sens. Environ.* **2018**, *204*, 244–259. [[CrossRef](#)]
56. Bhardwaj, A.; Sam, L.; Martín-Torres, F.J.; Zorzano, M.-P.; Fonseca, R.M. Martian slope streaks as plausible indicators of transient water activity. *Sci. Rep.* **2017**, *7*, 7074. [[CrossRef](#)]

57. Sam, L.; Bhardwaj, A.; Singh, S.; Kumar, R. Remote sensing flow velocity of debris-covered glaciers using Landsat 8 data. *Prog. Phys. Geogr. Earth Environ.* **2016**, *40*, 305–321. [[CrossRef](#)]
58. Sam, L.; Bhardwaj, A.; Kumar, R.; Buchroithner, M.F.; Martín-Torres, F.J. Heterogeneity in topographic control on velocities of Western Himalayan glaciers. *Sci. Rep.* **2018**, *8*, 12843. [[CrossRef](#)] [[PubMed](#)]
59. Singh, M.K.; Snehmani; Gupta, R.D.; Bhardwaj, A.; Joshi, P.K.; Ganju, A. High resolution DEM generation for complex snow covered Indian Himalayan Region using ADS80 aerial push-broom camera: A first time attempt. *Arab. J. Geosci.* **2015**, *8*, 1403–1414. [[CrossRef](#)]
60. Singh, M.K.; Gupta, R.D.; Snehmani; Bhardwaj, A.; Ganju, A. Scenario-based validation of moderate resolution DEMs freely available for complex Himalayan terrain. *Pure Appl. Geophys.* **2016**, *173*, 463–485. [[CrossRef](#)]
61. Snehmani; Bhardwaj, A.; Pandit, A.; Ganju, A. Demarcation of potential avalanche sites using remote sensing and ground observations: A case study of Gangotri glacier. *Geocarto Int.* **2014**, *29*, 520–535. [[CrossRef](#)]
62. Burrough, P.A.; McDonnell, R.A.; Lloyd, C.D. *Principles of Geographical Information Systems*, 3rd ed.; OUP: Oxford, UK, 2015; ISBN 978-0-19-874284-5.
63. Wilson, M.F.J.; O’Connell, B.; Brown, C.; Guinan, J.C.; Grehan, A.J. Multiscale Terrain Analysis of Multibeam Bathymetry Data for Habitat Mapping on the Continental Slope. *Mar. Geod.* **2007**, *30*, 3–35. [[CrossRef](#)]
64. De Smith, M.J.; Goodchild, M.F.; Longley, P. *Geospatial Analysis: A Comprehensive Guide to Principles, Techniques and Software Tools*; Troubador Publishing Ltd.: Leicester, UK, 2007; ISBN 978-1-905886-60-9.
65. Hong, I.-S.; Yi, Y.; Kim, E. Lunar pit craters presumed to be the entrances of lava caves by analogy to the Earth lava tube pits. *J. Astron. Space Sci.* **2014**, *31*, 131–140. [[CrossRef](#)]
66. Skinner, C.E. Open Vertical Volcanic Conduits: A Preliminary Investigation of an Unusual Volcanic Cave form with Examples from Newberry Volcano and the Central High Cascades of Oregon. In Proceedings of the Third International Symposium on Vulcanospeleology, Bend, OR, USA, 30 July–1 August 1982; pp. 7–17.
67. Fraedrich, W.; Heidari, N. *Iceland from the West to the South*; GeoGuide; Springer International Publishing: Cham, Switzerland, 2019; ISBN 978-3-319-90862-5.
68. Porter, C.; Morin, P.; Howat, I.; Noh, M.-J.; Bates, B.; Peterman, K.; Keesey, S.; Schlenk, M.; Gardiner, J.; Tomko, K.; et al. ArcticDEM 2018. Harvard Dataverse, V1 Type: Dataset. Available online: <https://dataverse.harvard.edu/dataset.xhtml?persistentId=doi:10.7910/DVN/OHHUKH> (accessed on 14 May 2020).
69. National Land Survey of Iceland web portal. Available online: <http://atlas.lmi.is/mapview/?application=DEM> (accessed on 4 June 2020).
70. ÍslandsDEM Útgáfa 0, Lýsigagnagátt. Available online: <https://gatt.lmi.is/geonetwork/srv/eng/catalog.search#/metadata/e6712430-a63c-4ae5-9158-c89d16da6361> (accessed on 4 June 2020).
71. Müller, D.; Walter, T.R.; Schöpa, A.; Witt, T.; Steinke, B.; Gudmundsson, M.T.; Dürig, T. High-resolution Digital Elevation Modeling from TLS and UAV campaign reveals structural complexity at the 2014/2015 Holuhraun eruption site, Iceland. *Front. Earth Sci.* **2017**, *5*. [[CrossRef](#)]
72. Swanson, D.A. Pahoehoe flows from the 1969–1971 Mauna Ulu eruption, Kilauea volcano, Hawaii. *Gsa Bull.* **1973**, *84*, 615–626. [[CrossRef](#)]
73. Kilburn, C.R.J. Lava Flows and Flow Fields. In *Encyclopedia of Volcanoes*; Academic Press: San Diego, CA, USA, 2000; pp. 291–305.
74. Murcia, H.; Németh, K.; Moufti, M.R.; Lindsay, J.M.; El-Masry, N.; Cronin, S.J.; Qaddah, A.; Smith, I.E.M. Late Holocene lava flow morphotypes of northern Harrat Rahat, Kingdom of Saudi Arabia: Implications for the description of continental lava fields. *J. Asian Earth Sci.* **2014**, *84*, 131–145. [[CrossRef](#)]
75. Hon, K.; Johnson, J.; Gansecki, C.A. *Field Interpretation of Active Volcanoes: A Handbook for Viewing Lava*; Reveira, T., Ed.; Hawaii U.S: Geological Survey Hawaiian Volcano Observatory: Hilo, Hawaii, 2008.
76. Pedersen, G.B.M.; Höskuldsson, A.; Riishuus, M.S.; Jónsdóttir, I.; Gudmundsson, M.T.; Sigmundsson, F.; Óskarsson, B.V.; Drouin, V.; Gallagher, C.; Askew, R.; et al. Nornahraun Lava Morphology and Mode of Emplacement. In Proceedings of the EGU General Assembly Conference, Vienna, Austria, 12–17 April 2015; Volume 17, p. 11958.
77. Rowland, S.K.; Walker, G.P.L. Toothpaste lava: Characteristics and origin of a lava structural type transitional between pahoehoe and aa. *Bull. Volcanol.* **1987**, *49*, 631–641. [[CrossRef](#)]
78. Walker, G.P.L. Structure, and origin by injection of lava under surface crust, of tumuli, “lava rises”, “lava-rise pits”, and “lava-inflation clefts” in Hawaii. *Bull. Volcanol.* **1991**, *53*, 546–558. [[CrossRef](#)]

79. Kempe, S. Chapter 131—Volcanic Rock Caves. In *Encyclopedia of Caves*, 3rd ed.; White, W.B., Culver, D.C., Pipan, T., Eds.; Academic Press: Cambridge, MA, USA, 2019; ISBN 978-0-12-814124-3.
80. Kempe, S. Principles of Pyroduct (Lava Tunnel) Formation. In Proceedings of the 15th International Congress of Speleology, Kerrville, TX, USA, 19–26 July 2009.
81. Opheim, J.A.; Gudmundsson, A. Formation and geometry of fractures, and related volcanism, of the Krafla fissure swarm, northeast Iceland. *Gsa Bull.* **1989**, *101*, 1608–1622. [[CrossRef](#)]
82. Crown, D.A.; Ramsey, M.S. Morphologic and thermophysical characteristics of lava flows southwest of Arsia Mons, Mars. *J. Volcanol. Geotherm. Res.* **2017**, *342*, 13–28. [[CrossRef](#)]
83. Cushing, G.E.; Okubo, C.H.; Titus, T.N. Atypical pit craters on Mars: New insights from THEMIS, CTX, and HiRISE observations. *J. Geophys. Res. Planets* **2015**, *120*, 1023–1043. [[CrossRef](#)]
84. Mars Global Cave Candidate Catalog—ScienceBase-Catalog. Available online: <https://www.sciencebase.gov/catalog/item/5bd36eb1e4b0b3fc5ce51783> (accessed on 6 June 2020).
85. Cushing, G. Candidate cave entrances on Mars. *J. Cave Karst Stud.* **2012**, *74*, 33–47. [[CrossRef](#)]
86. A Volcanic Fissure. Available online: <http://www.nasa.gov/image-feature/jpl/pia21601/a-volcanic-fissure> (accessed on 1 June 2020).
87. Wilson, L.; Mouginis-Mark, P.J.; Tyson, S.; Mackown, J.; Garbeil, H. Fissure eruptions in Tharsis, Mars: Implications for eruption conditions and magma sources. *J. Volcanol. Geotherm. Res.* **2009**, *185*, 28–46. [[CrossRef](#)]
88. Wynne, J.J.; Titus, T.N.; Chong Diaz, G. On developing thermal cave detection techniques for earth, the moon and mars. *Earth Planet. Sci. Lett.* **2008**, *272*, 240–250. [[CrossRef](#)]



© 2020 by the authors. Licensee MDPI, Basel, Switzerland. This article is an open access article distributed under the terms and conditions of the Creative Commons Attribution (CC BY) license (<http://creativecommons.org/licenses/by/4.0/>).